CENTRO BRASILEIRO DE PESQUISAS FÍSICAS

---

**Coordenação de Matéria Condensada, Física Aplicada e Nanociência (COMAN)**

**Master Dissertation in Physics**

# QUANTIFICATION OF TWO FLUIDS IN POROUS MEDIA USING NUCLEAR MAGNETIC RESONANCE

Mariana Teixeira de Azevedo

**Rio de Janeiro**
**2025**

# QUANTIFICATION OF TWO FLUIDS IN POROUS MEDIA USING NUCLEAR MAGNETIC RESONANCE

**Mariana Teixeira de Azevedo**

Master's Dissertation submitted to the Scientific Training Coordination of the Brazilian Center for Research in Physics (CBPF) as part of the requirements for obtaining the degree of Master in Physics.

Advisor: Prof. Dr. Ivan de Oliveira
Co-advisor: Dr. Moacyr Nascimento

Rio de Janeiro
2025

1949 | 2024 75 ANOS CBPF

César Lattes 100 ANOS 1924 | 2024

MINISTÉRIO DA
CIÊNCIA, TECNOLOGIA
E INOVAÇÃO

GOVERNO FEDERAL
BRASIL
UNIÃO E RECONSTRUÇÃO

# "QUANTIFICATION OF TWO FLUIDS IN POROUS MEDIA USING NUCLEAR MAGNETIC RESONANCE"

## MARIANA TEIXEIRA DE AZEVEDO

Dissertação de Mestrado em Física apresentada no Centro Brasileiro de Pesquisas Físicas do Ministério da Ciência Tecnologia e Inovação. Fazendo parte da banca examinadora os seguintes professores:

Ivan

Ivan S. Oliveira - Orientador/CBPF

Documento assinado digitalmente
gov.br
MOACYR SILVA DO NASCIMENTO NETO
Data: 13/05/2025 09:54:59-0300
Verifique em https://validar.iti.gov.br

Moacyr S. Nascimento – Coorientador/ CENPES

Documento assinado digitalmente
gov.br
JAIR CARLOS CHECON DE FREITAS
Data: 20/02/2025 18:25:07-0300
Verifique em https://validar.iti.gov.br

Jair C. C. Freitas - UFES

Documento assinado digitalmente
gov.br
TITO JOSE BONAGAMBA
Data: 21/02/2025 13:33:09-0300
Verifique em https://validar.iti.gov.br

Tito J. Bonagamba – USP – SÃO CARLOS

Rio de Janeiro, 19 de fevereiro de 2025.

---

**Centro Brasileiro de Pesquisas Físicas**
Rua Doutor Xavier Sigaud, 150, URCA, Rio de Janeiro, Brasil
Tel.: +55 21 2141-7100     CEP:22290-180
http://www.cbpf.br

*To all the good friends we make along the way,*
*for whom I could make friendship bracelets to celebrate.*

*And to everyone who puts their whole heart and soul*
*into something, only to be met with cynicism,*
*skepticism, resistance, or negativity—this probably*
*means you're doing something new.*

# Acknowledgement

Certainly, I will never find enough words to express my gratitude to Professor Dr. Ivan. Thank you for believing in me, for trusting me, and for giving me the opportunity to pursue the best master's degree I could have imagined, even when I was nothing more than an undergraduate Physics student. Your unwavering confidence and support during every meeting, in every result I presented, and your constant willingness to let me be myself were essential throughout this journey. Above all, thank you for being the ideal advisor—someone who not only guides but also inspires. This research and my experience during this master's program would not have been the same without you.

I also want to express my immense gratitude to Alexsandro, who has been by my side from day one, holding my hand and teaching me every detail of what I know today. Thank you for trusting every step I took, for being present every single day in the lab, sharing both the work and the companionship. If you hadn't given me this chance, none of this—this dissertation, the award, or everything I've achieved—would have been possible. Your generosity and patience have changed my life, and I will be forever grateful for that.

To my co-advisor, Moacyr, my gratitude for opening the doors beyond of the academic world to me. Thank you for encouraging me, welcoming me, and for all the opportunities and inspiring conversations along the way. Your support was a fundamental pillar in the realization of this research.

To my family, my foundation, and my greatest example of resilience, thank you for everything. Especially to my mother: being a woman in a predominantly male world is not easy, but you face every challenge with courage and determination. That's why I admire you so much. Thank you for being my inspiration and for teaching me never to give up, even in the face of difficulties.

To my friends, my second family, my heart overflows with gratitude for you. A special thanks to the friends UERJ gave me: Vitor Gozzi, Gustavo Levy, Patrick Belmont, Diego Rigo, Gabs, and Helena. If friends are the family we choose, then I've been more than

lucky. Thank you for being with me through every moment, sharing this life in such a special way. You are the least dysfunctional and happiest family I could ever have, and I would choose all of you, every day, always.

Lastly, to Murilo: they say it's possible to live a lifetime and never find the love of your life within it, but I've been privileged. Thank you for all the support since the day we met. For the countless sleepless nights listening to my frustrations, the sunny afternoons of celebration, the lazy mornings, and all the days hearing me talk about everything I love. There's no world or reality where ”we” don't exist. Our bond goes far beyond that, and you know it. I'll never have words to thank you for the fairy tale you've made of my life. No fictional character comes close to the reality you give me—even if, at the end of the day, I never let you have any peace. You are my ”happily ever after” and ”whatever ends” all at once.

Everything you lose is a step you take
So make the friendship bracelets
Take the moment and taste it
You’ve got no reason to be afraid
You’re on your own, kid
Yeah, you can face this
You’re on your own, kid
You always have been.
*Taylor Swift*

# Abstract

We present a robust methodology for the quantitative analysis of two immiscible fluids—water and oil—within synthetic porous media using advanced Nuclear Magnetic Resonance (NMR) techniques. This work aims to enhance the characterization of multiphase fluid distribution by integrating high-resolution NMR imaging with rigorous statistical petrophysical analysis.

The methodology comprises three key stages: (1) fabrication of synthetic porous samples via sintering of soda-lime glass microspheres, selected for their physicochemical similarity to natural reservoir rocks; (2) controlled saturation of the samples under vacuum and pressure conditions to emulate realistic subsurface fluid configurations; and (3) fluid identification and quantification using NMR imaging, employing both chemical shift and relaxation contrast mechanisms to distinguish between water and oil distributions within the pore network.

Quantitative analysis was performed through a custom Python-based image processing algorithm that extracts pixel intensity histograms from $T_2$-weighted NMR images, enabling precise determination of relative fluid content. This approach yielded an average quantification error below 10% across a range of sample conditions, underscoring the method's accuracy and reproducibility.

Our findings validate the efficacy of combining NMR imaging and advanced data analytics for fluid characterization in porous systems. The proposed methodology offers a scalable framework for applications in reservoir engineering, environmental remediation, and materials science, while also highlighting future challenges in adapting the technique for real-time industrial deployment. This work opens avenues for integrating physics-based imaging with computational tools to advance the understanding of multiphase flow in complex porous structures.

**Keywords:** Nuclear Magnetic Resonance, porous media, fluid quantification, $T_2$-weighted imaging, reservoir engineering.

# Resumo

Este trabalho apresenta uma metodologia robusta para a quantificação de dois fluidos imiscíveis — água e óleo — em meios porosos sintéticos, utilizando técnicas avançadas de Ressonância Magnética Nuclear (RMN). O objetivo é aprimorar a caracterização da distribuição multifásica de fluidos por meio da integração de imagens de alta resolução por RMN com análise estatística petrofísica rigorosa.

A metodologia foi estruturada em três etapas principais: (1) produção de amostras porosas sintéticas por sinterização de microesferas de vidro sodocálcico, selecionadas por sua semelhança físico-química com rochas reservatório naturais; (2) saturação controlada das amostras sob condições de vácuo e pressão, simulando a disposição de fluidos em ambientes subsuperficiais; e (3) identificação e quantificação dos fluidos por imagem de RMN, explorando mecanismos de contraste por deslocamento químico e relaxação para distinguir com precisão a distribuição de óleo e água na rede de poros.

A quantificação foi realizada por meio de um algoritmo de processamento de imagem desenvolvido em Python, que analisa histogramas de intensidade de pixels extraídos de imagens ponderadas em $T_2$. Essa abordagem permitiu determinar com alta precisão a proporção relativa dos fluidos, com margem média de erro inferior a 10%, demonstrando elevada acurácia e reprodutibilidade.

Os resultados validam a eficácia da metodologia proposta, oferecendo uma base sólida para aplicações em engenharia de reservatórios, remediação ambiental e ciência de materiais. Além disso, este estudo evidencia o potencial da integração entre técnicas de imagem física e ferramentas computacionais para o avanço do entendimento do escoamento multifásico em meios porosos complexos, ao mesmo tempo em que aponta os desafios para sua adaptação em contextos industriais em tempo real.

**Palavras-chave:** Ressonância Magnética Nuclear, meios porosos sintéticos, quantificação de fluidos, imagens pesadas em $T_2$, engenharia de reservatórios.

# List of Figures

# List of Tables

# Contents

# Introduction

Porous media are materials whose significance arises from their intricate internal structures, where features such as microstructures and macroporosity play a crucial role in determining their physical, chemical, and biological properties [1]. These structures often consist of conglomerates of grains, fibers, or solids organized into networks of interconnected or isolated pores that directly influence the performance and functionality of these materials. Porous media are ubiquitous in nature and daily life, exemplified by materials such as rocks, wood, soil, biological tissues, and bones [2].

Nuclear magnetic resonance (NMR) has emerged as a powerful tool for studying porous media since the 1950s when Felix Bloch first demonstrated its potential [3]. Bloch observed that fluids within pores generate detectable NMR signals, enabling direct analysis of the properties of these systems through relaxation, diffusion, flow, and imaging experiments. Using significantly simpler equipment than is available today, Bloch established a fundamental relationship between pore relaxation surfaces and NMR signals, opening new avenues for porous media characterization [4].

Technological advancements over the past decades have made NMR an essential tool for the non-invasive characterization of porous materials. Its applications range from studying fluid transport in rocks and soils—critical for geological exploration—to analyzing biological tissues for medical diagnostics [5]. The integration of physics, chemistry, and engineering advances has given rise to magnetic resonance in porous media (MRPM), significantly expanding the frontiers of this research field [6].

Within this context, petrophysics plays a pivotal role, focusing on rocks' physical and chemical properties and their interactions with contained fluids. Among its primary applications is the analysis of hydrocarbon reservoirs, where NMR has proven to be an indispensable tool [7]. This technique enables the investigation of fluid-filled porous media, providing essential information on properties such as porosity, permeability, and fluid behavior at the microscopic scale. Consequently, the synergy between NMR and petrophysics has driven significant advancements in understanding and characterizing natural and synthetic porous systems [8].

The cumulative knowledge in petrophysics, NMR, and porous media has been instrumental in developing and enhancing petroleum industries. These industries extensively apply these concepts in exploring and extracting petroleum from reservoirs, including offshore environments. However, despite considerable scientific and technical progress, significant challenges remain in the extraction process of the world's most utilized energy source: petroleum [9].

Among these challenges are the precise identification of oil reservoirs and the efficiency of extraction processes. This study, in particular, focuses on quantifying two fluids present in porous media using NMR techniques [10]. Determining the quantities of fluids, especially oil and water, within these rocks is critical for evaluating the economic feasibility of exploration. Reservoirs with low oil saturation often do not justify the high extraction costs, making a detailed analysis of these porous systems' conditions essential for decision-making [11].

Thus, this research aims to contribute to a better understanding and optimization of quantification techniques, aiding in decision-making regarding petroleum extraction in reservoirs with complex characteristics.

Chapter 1 addresses the operation of nuclear magnetic resonance equipment, beginning with its basic principles. It then introduces concepts such as relaxation, relaxation times ($T_1$ and $T_2$), the image acquisition process, and the application of pulses required to characterize the studied materials.

Chapter 2 explores the field of petrophysics and porous media, discussing fundamental concepts such as porosity and permeability while examining the essential properties of these materials and their behavior in various contexts.

Chapter 3 provides a detailed description of the methodology used in this study. It encompasses the sintering process of synthetic porous rocks and the procedures for saturating these samples with fluids, highlighting the experimental steps required for the investigation.

Chapter 4 is dedicated to discussing the obtained results. It presents the analyses based on NMR-acquired images, the fluid quantification process, and the study's main findings. Additionally, it elaborates on the interpretations drawn from the methodology and the generated data.

Finally, the conclusion presents a combination of the results achieved while highlighting the advantages and limitations of the proposed NMR-based fluid quantification method. It also suggests perspectives for future studies and potential improvements to the used approach.

This work also includes an Appendix, which provides additional information about the samples studied during the master's research. These details support the results obtained and enhance the credibility of the developed methodology.

This dissertation also includes a chapter on Events and Conferences, providing a detailed overview of the academic events attended during the master's program. These experiences facilitated the dissemination of research findings, engagement with experts, and the expansion of the academic network.

# Chapter 1

# Nuclear Magnetic Resonance

In 1946, Felix Bloch and Edward Purcell independently discovered the phenomenon and recognized it as the basis for identifying magnetic resonance (MR). While Purcell was investigating the properties of solids at Harvard University, Bloch focused his studies on liquids at Stanford University ([12]; [13]). Earlier, in 1937, Isidor Rabi, a physics professor at Columbia University, conducted the first nuclear magnetic resonance experiment using an atomic beam. This work earned him the 1944 Nobel Prize in Physics for creating a "method for recording the magnetic resonance properties of atomic nuclei." Between the 1950s and 1970s, MR established itself as an essential tool for molecular, physical, and chemical analyses [14].

In parallel, during the 1960s, McCall, Douglas, and Anderson proposed the concept of using field gradients to study diffusion and fluids through a series of works. However, the formalization and demonstration of these principles occurred only in 1965 with the publication of the paper "Spin Diffusion Measurements: Spin Echoes in the Presence of Time-Dependent Field Gradient" by E. O. Stejskal and J. E. Tanner [15].

The chemical and structural analysis of solids and liquids initially relied on magnetic resonance techniques. Later, in the 1970s, Paul Lauterbur and Peter Mansfield made groundbreaking contributions to the development of magnetic resonance imaging (MRI), expanding on the principles of NMR to explore living tissues. Their work demonstrated the ability to differentiate normal and abnormal tissues based on distinct signals, sparking interest in medical imaging.

Lauterbur introduced the concept of creating two-dimensional images by using magnetic field gradients, which made it possible to determine the origin of radiofrequency waves emitted by atomic nuclei within a sample [16]. Mansfield, on the other hand, developed slice-selection techniques and advanced the understanding of how NMR signals could be processed to construct high-resolution images [17].

In recognition of their revolutionary contributions, Lauterbur and Mansfield were awarded the 2003 Nobel Prize in Physiology or Medicine for creating a non-invasive imaging method capable of producing highly detailed anatomical images, which replaced numerous traditional diagnostic techniques [18].

## 1.1 Concepts of Nuclear Magnetic Resonance

The interaction between atomic nuclei and an externally applied magnetic field forms the basis of Nuclear Magnetic Resonance [19]. An atom consists of three fundamental particles: protons, which carry a positive charge; neutrons, which are electrically neutral; and electrons, which have a negative charge. Protons and neutrons remain confined to the atomic nucleus, while electrons orbit around it.

The phenomenon of NMR arises from the interaction between particles possessing angular momentum (spin) and magnetic moment when exposed to an external magnetic field [20]. Among the various nuclei that exhibit NMR properties, hydrogen ($^1$H) plays a fundamental role due to its high natural abundance and significance in organic chemistry. In NMR the hydrogen is the primary nucleus utilized for three main reasons:

1. It is the most abundant element in the human body, constituting approximately 10% of body weight [21].
2. The NMR properties of hydrogen allow for distinct differentiation between normal and pathological tissues [16].
3. The hydrogen proton possesses the highest magnetic moment among biologically relevant nuclei, making it the most sensitive to NMR detection [22].

In the context of NMR, the spin quantum number ($I$) of hydrogen is $1/2$, meaning that it has two possible orientations when subjected to an external magnetic field: parallel (low-energy state) and antiparallel (high-energy state). These orientations correspond to distinct energy levels governed by the principles of quantum mechanics [23].

In the absence of an external magnetic field, the magnetic moments of hydrogen nuclei are randomly oriented. However, when placed within a strong magnetic field, these nuclei align either parallel or antiparallel to the field direction. The distribution of spins between these two energy states follows the Boltzmann distribution (1.1), with a slight excess of nuclei occupying the lower-energy state [24]. This slight population imbalance is the basis for the detectable NMR signal.

$$\frac{N_P}{N_{AP}} = e^{-E/kT}, \tag{1.1}$$

where $N_P$ is the number of spins aligned parallelly; $N_{AP}$ is the number of spins aligned anti-parallelly; $k$ is Boltzmann constant and $T$ is absolute temperature, in kelvin.

In an attempt to align with the applied magnetic field and due to their intrinsic spin, which can be classically visualized as a continuous rotation around their axis, this additional motion known as precession. This rotation imparts a magnetic moment ($\mu$) to the nuclei, allowing them to interact in a specific way with external magnetic fields ($B_0$). The intensity of this interaction is described by the gyromagnetic ratio ($\gamma$), a constant that determines the characteristic precession frequency of the nuclei around the applied magnetic field, known as the Larmor frequency ($\omega_0$). The Larmor equation (1.2) expresses this relationship:

$$\omega_0 = \gamma B_0. \tag{1.2}$$

A notable characteristic of the Larmor frequency is particular of each nuclear isotope. This specificity makes NMR equipment indispensable tools for the study of virtually all elements in the periodic table, except argon and cerium[1]. In the study presented in this work, the nuclide of most significant interest is hydrogen ($^1$H), with a gyromagnetic ratio of approximately $42 MHz/T$.

Applying this equipment as a spectroscopic technique for nuclide analysis, combined with manipulating nuclear spins and studying relaxation phenomena, enabled the development of magnetic resonance imaging. This revolutionary technique allowed for the mapping of different biological tissues, thanks to variations in the relaxation times of nuclei, which depend directly on the chemical environment in which they are embedded.

The functioning of NMR can be illustrated by considering a sample without an external magnetic field. In this state, the sample magnetic moments are disordered. As a result, the system does not show total magnetization ($M_T$) since the vector sum of the

---

[1] These two elements are examples of those that lack naturally abundant isotopes with a non-zero nuclear spin. As a result, they do not exhibit measurable interactions with external magnetic fields during NMR experiments, rendering them effectively invisible to this technique.

individual magnetic moments is zero.

When the sample is placed in the NMR equipment, a static magnetic field $B_0$ is applied, inducing the alignment of the nuclear spins in the direction of this field. This alignment generates a non-zero macroscopic magnetization in the system, represented by $M_0$. As mentioned earlier, when the spins are under the influence of a magnetic field, they precess around the direction of the field at a characteristic frequency known as the Larmor frequency ($\omega_0$). This behavior occurs due to the interaction between the nuclear magnetic moments and the external field [25].

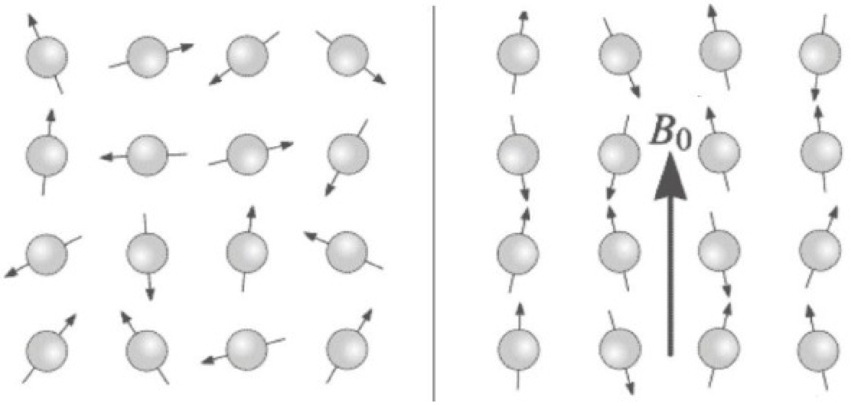

Figure 1.1: Effect of applying a static magnetic field $B_0$ to a system of nuclei with non-zero spins. After the application of the field, the system acquires a total magnetization $M_0$ different from zero.

A second time-dependent magnetic field, $B_1$, is applied to manipulate the magnetization. This field has a lower intensity than $B_0$ and is tuned to the frequency $\omega_0$ of the protons in the sample. The field is emitted as radiofrequency pulses, oriented orthogonally to $B_0$. When the protons absorb the energy from this resonant pulse, a change in the direction of $M_0$ occurs, moving it away from its equilibrium position. If we allow this $B_1$ field pulse to be sufficiently long, the magnetization, initially aligned with the Z-axis, is completely displaced to the XY plane, becoming perpendicular to both $B_0$ and $B_1$, resulting in a pulse known as $\frac{\pi}{2}$ pulse [26].

When the $B_1$ field is turned off, the protons begin the realignment process, gradually returning to their original equilibrium orientation. During this interval, they emit energy at the frequency $\omega_0$, corresponding to the Larmor frequency. At the same time, the $M_0$ precesses around the $B_0$ field, exhibiting behavior similar to a gyroscope spinning around its vertical axis.

This precessional motion of the magnetization out of equilibrium generates a signal known as free induction decay (FID) [27]. The initial magnitude of the FID signal directly depends on the value of $M_0$ immediately after applying the 90° pulse. Over time, the signal decays due to the gradual release of the energy absorbed by the protons, a process known as relaxation. Additionally, there is a loss of coherence between the protons, contributing to decreased detected signal. An example of a FID can be seen in the Figure [1.2].

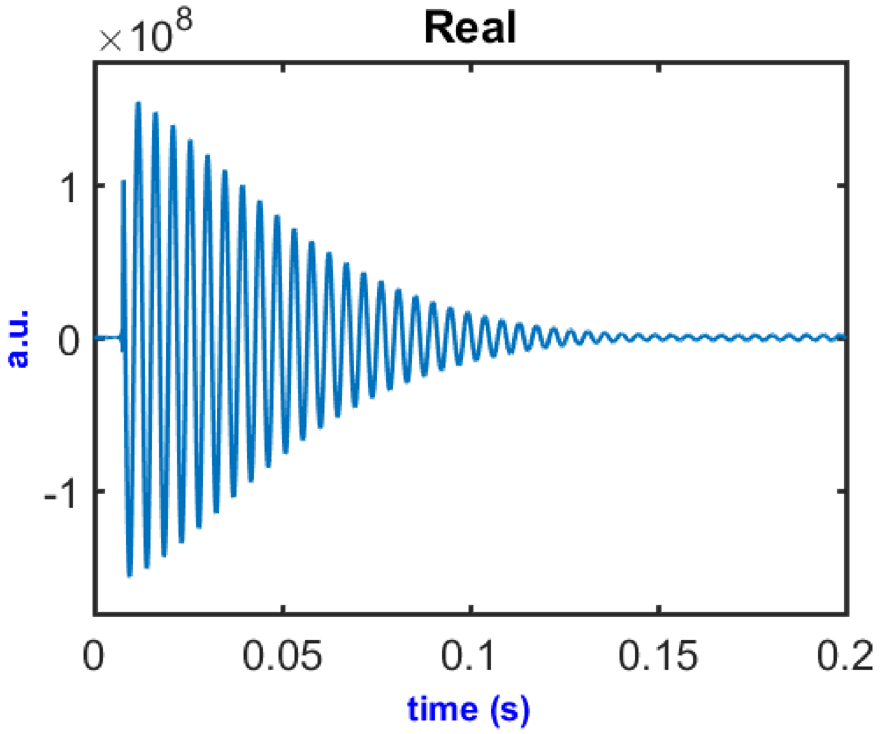

Figure 1.2: Free Induction Decay (FID) signal, showing the real component of the NMR response over time. The signal exhibits an oscillatory decay due to transverse relaxation effects.

In most situations, the FID signal exhibits varying overlapping frequencies, making direct analysis in the time domain difficult and complex. In this context, analyzing these multiple signals in the frequency domain rather than the time domain is much more practical. A mathematical operation known as the Fourier transform converts time-domain signals to frequency-domain signals.

## 1.2 Relaxation

While Magnetic Resonance measurements can be analyzed regarding the transferred energy, the relaxation phenomenon refers to the process by which each proton releases the energy it initially absorbed, provided in the form of radiofrequency pulses. As one of the fundamental processes of NMR, this energy release is essential for forming the contrast imaging mechanism [22].

As previously mentioned, protons can only absorb radiofrequency energy when emitted at the correct frequency. After excitation, the system enters the relaxation process, during which each proton gradually releases the absorbed energy and naturally returns to its equilibrium configuration, accompanied by the precession of the spins around the magnetic field.

As remarked before, Bloch formulated the relationships that describe the behavior of the components of the nuclear magnetization vector, $M_T$, under the interaction with the magnetic field, $B_0$, including the relaxation terms. These equations are given as follows:

$$\frac{dM_x}{dt} = \gamma \left(M_y B_z - M_z B_y\right) - \frac{M_x}{T_2}, \tag{1.3}$$

$$\frac{dM_y}{dt} = \gamma \left(M_z B_x - M_x B_z\right) - \frac{M_y}{T_2}, \tag{1.4}$$

$$\frac{dM_z}{dt} = \gamma \left(M_x B_y - M_y B_x\right) - \frac{M_z - M_0}{T_1}, \tag{1.5}$$

where $B_x$, $B_y$, and $B_z$ are the components of the magnetic field $B_0$; $T_1$ is the longitudinal relaxation time; $T_2$ is the transverse relaxation time; and $M_0$ is the equilibrium magnetization. These equations are fundamental for understanding both longitudinal and transverse magnetization, which will be discussed in Sections [1.2.1] and [1.2.2], respectively.

An essential feature of relaxation is that, although energy absorption occurs individually for each proton, the relaxation time is measured globally, considering the collective response of the entire sample. This approach allows the calculation of the average response of the protons present in the sample. Two distinct relaxation times can be measured based on the final destination of the energy released during the process, known as $T_1$ and $T_2$.

### 1.2.1 $T_1$ Relaxation

The relaxation time $T_1$ can be described by the fact that, after a spin excitation, the absorbed energy is transferred to the surrounding environment, called the lattice, rather than transferred directly to the other spins. This energy exchange process no longer contributes to the excitation of other spins, which is why this relaxation time is also known as the spin-lattice relaxation time. Another term used to describe $T_1$ is longitudinal relaxation time, which refers to the time required for the longitudinal magnetization component ($M_z$) to return to 63% of its original value after applying an excitation pulse [28].

This relaxation time enables a mechanism in which each spin donates its energy to the lattice to return to its equilibrium orientation. For example, longitudinal magnetization is not immediately observed when a 90° pulse is applied to a sample. However, the longitudinal magnetization begins to be detected over time as the protons start releasing their energy. This process follows an exponential growth, with the time constant $T_1$ characterizing this growth rate. The following equation (1.6) can describe this behavior:

$$M(t) = M_0(1 - e^{-t/T_1}), \tag{1.6}$$

where $M_T$ is the magnetization over time ($t$) after the application of the radiofrequency pulse, and $T_1$ is the longitudinal relaxation time, which describes the rate at which the magnetization along the external magnetic field ($B_0$) recovers after excitation (this $T_1$ relaxation can be observed in Figure [1.3]).

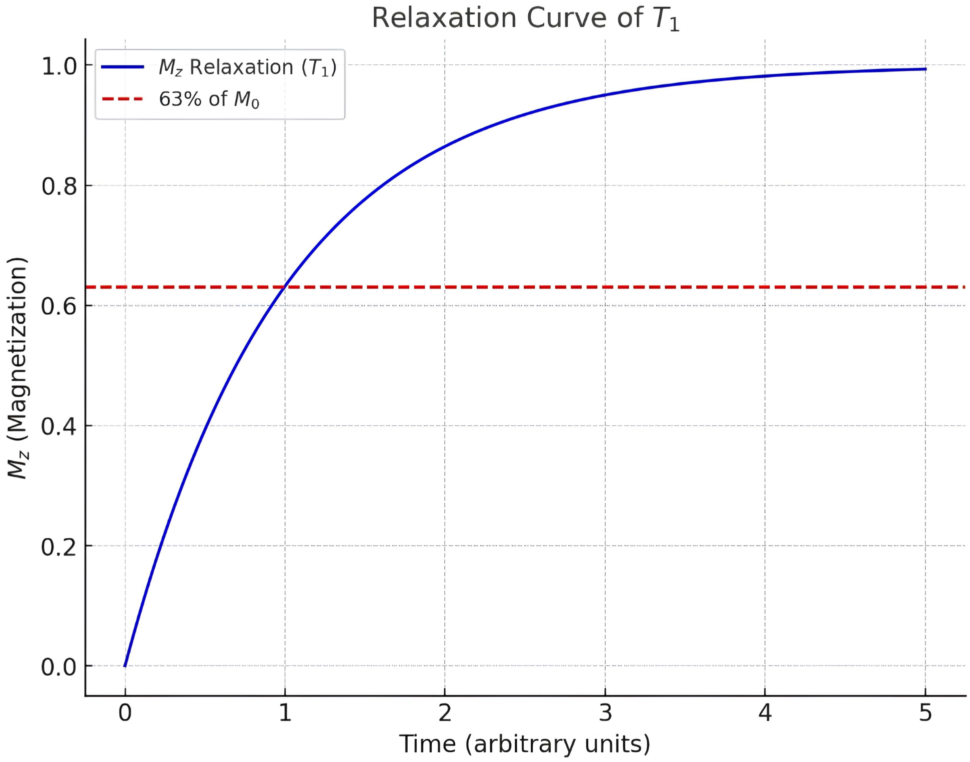

Figure 1.3: $T_1$ relaxation curve, representing the longitudinal recovery of magnetization ($M_z$) over time. The dashed red line marks 63% of the equilibrium magnetization ($M_0$), indicating the characteristic relaxation time $T_1$.

After some time approximately equal to five times the longitudinal relaxation time ($T_1$), the magnetization returns to about 99.3% of its original value, i.e., to the state it had before the application of the excitation pulse [20]. This process is known as $T_1$ recovery. We can express this behavior mathematically using the following equation (1.7):

$$M(5T_1) = M_0(1 - e^{-5}) \approx 0.993M_0 \tag{1.7}$$

The energy dissipated to the surroundings has important implications, as this effect is responsible for the relaxation of protons. When a pulse is applied consecutively, preventing proper relaxation, $T_1$ saturation occurs. This technique is widely used in MRI to generate images with better contrast based on differences in longitudinal relaxation ($T_1$) [29].

The magnetization along the Z-axis increases with the applied magnetic field, enhancing the signal up to a saturation limit. However, $T_1$ relaxation, which describes the return of magnetization to equilibrium, is influenced by the strength of the magnetic field. In stronger fields, the $T_1$ relaxation time becomes longer, increasing the risk of saturation. Consequently, while a stronger magnetic field might initially improve signal strength, it can also delay the recovery of spins to their equilibrium state, potentially affecting the overall signal quality [30].

The $T_1$ relaxation time is independent of the application of the RF pulses, since it depends solely on the interactions between the spins and their surrounding lattice. To obtain a higher-quality signal, it is crucial to optimize energy absorption by matching the applied frequency as closely as possible to the resonance frequency of the nuclei [31]. This ensures efficient energy transfer between the magnetic field and the proton spins, enhancing the overall signal strength without altering the $T_1$ relaxation time.

### 1.2.2 $T_2$ Relaxation

A fundamental difference between the two relaxations is how each responds after applying a radiofrequency pulse. In the case of $T_2$ relaxation, also known as spin-spin relaxation, the energy of an excited proton is transferred directly to the nearest proton. Overall, the energy stays within the spin system, continuously exchanging between neighboring protons.

This energy transfer can occur repeatedly as long as the protons are close to each other and undergoing precession at approximately the same frequency. However, since the interaction occurs exclusively and strongly between spins, without involving energy dissipation into the environment (the lattice), $T_2$ is often shorter than $T_1$. It is mainly determined by the homogeneity of the magnetic field and the local interactions between the spins; in this case, it is referred to as $T_2^*$ [32]. The following equation (1.8) can describe this behavior:

$$M(t) = M_0 e^{-t/T_2}, \tag{1.8}$$

where $M_T$ is the magnetization over time $(t)$ after the application of the radiofrequency pulse, and $T_2$ is the transverse relaxation time, which describes the rate at which the magnetization along the external magnetic field $(B_0)$ recovers after excitation.

Another way to define $T_2$ is as the transverse relaxation time, as it represents the time required for the transverse component of the magnetization to decay to 37% of its initial value [23]. In an equilibrium system, $M_T$ is aligned with the Z-axis of $B_0$ as can be observed in the Figure [1.4].

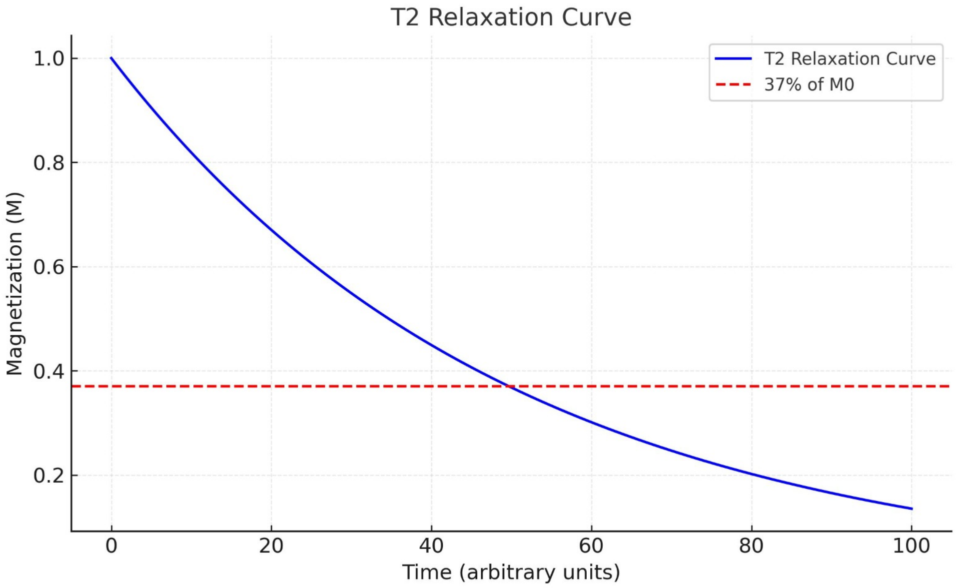

Figure 1.4: $T_2$ relaxation curve, representing the transverse decay of magnetization ($M$) over time. The dashed red line indicates 37% of the initial magnetization ($M_0$), making the characteristic relaxation time $T_2$.

When a 90° pulse is applied, the magnetization $M_T$ is entirely rotated to the XY plane, aligning all spins in this plane. This alignment is called coherence, resulting in total magnetization in the transverse plane.

However, after the 90° pulse ends, the spins begin to release the absorbed energy as time progresses. Due to spin-spin interactions, the protons exchange energy while reorienting in the XY plane, leading to the loss of coherence. This event results in the FID signal. For this reason, the time $T_2$ or $T_2^*$ [2] is defined as the process by which transverse magnetization is lost.

An important point is that $T_2^*$ is the rate at which transverse magnetization decays due to inhomogeneities in the main magnetic field. These inhomogeneities can be caused by intrinsic defects in the magnet or field distortions that tissues generate. In contrast, $T_2$ is the ”natural” or ”true” rate of the sample being analyzed. Therefore, $T_2^*$ represents the rate at which transverse magnetization decays meaning it is always less than or equal to $T_2$ [33].

Since all magnetic fields exhibit inhomogeneities, an appropriate pulse sequence is used to obtain a value closer to $T_2$ rather than $T_2^*$. This allows for the correction of dephasing caused by magnetic field inhomogeneities, eliminating effects related to field

---

[2] when additional factors, such as magnetic field inhomogeneities, are involved

gradients. A classic example of this approach is the spin-echo technique, which uses additional pulses to reverse the accumulated phase shift and partially recover the signal [34].

## 1.3 Chemical Shift

Chemical shifts in NMR refer to the phenomenon where the resonant frequency of a nucleus in a magnetic field is influenced by its chemical environment. This effect arises from the shielding or deshielding of the nucleus by the surrounding electron cloud. When a nucleus experiences different local electron densities due to nearby atoms or groups, its resonant frequency is altered relative to a reference standard. In this way, the position and value of the chemical shift can be used to characterize molecule's structure [24]. The Figure [1.5] is a typical example of a chemical shift spectrum in NMR. It shows signals at different ppm values, corresponding to different chemical environments in the analyzed compound.

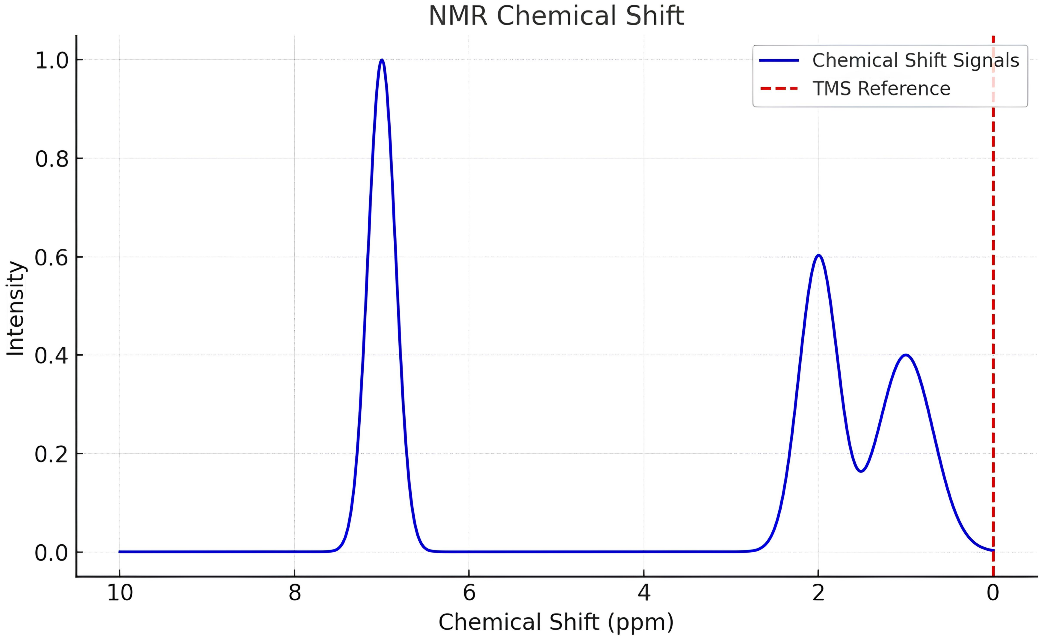

Figure 1.5: NMR chemical shift spectrum, showing intensity as a function of chemical shift (ppm). The blue peaks represent chemical shift signals, while the red dashed line marks the TMS reference signal.

The magnitude of this shift is expressed in parts per million (ppm) and is known as the chemical shift. Tetramethylsilane (TMS), is commonly used as the standard for determining the chemical shift of compounds, with $\delta TMS = 0ppm$. In other words, the frequencies for chemicals are measured for a ($^1$H) nucleus of a sample relative to the ($^1$H) resonance of TMS. This allows the chemical structure of a molecule to be characterized based on the chemical shift values of the nuclei in the molecule [35]. This chemical shift can be calculated using the following equation (1.9):

$$\delta = \frac{\upsilon_{sample} - \upsilon_{ref}}{\upsilon_{ref}}, \tag{1.9}$$

where $\upsilon_{\text{sample}}$ is the absolute resonance frequency of the sample, $\upsilon_{\text{ref}}$ is the absolute resonance frequency of a standard reference compound, and $\delta$ is expressed in ppm (parts per million).

## 1.4 Principles of Magnetic Resonance Imaging

Magnetic resonance imaging is based on the dependence of the resonance frequencies with the applied magnetic field. The application of magnetic field gradients makes this process possible [29].

Gradients are small perturbations superimposed on the main $B_0$, introducing a controlled spatial variation in the field intensity [36]. This variation is exceptionally subtle, representing less than 1% of the total value of $B_0$. However, it is sufficient to differentiate the resonance frequencies of protons along specific directions, enabling the spatial encoding necessary to form detailed images [37].

Gradients can be applied along the X, Y, and Z directions (see more in the figure [1.6]), and each can be controlled through software. These gradients allow obtaining slices, frequency encoding, and phase encoding. The selective application of gradients allows the isolation and analysis of different regions of the object under study, making it possible to generate detailed images of cross-sectional areas or specific planes [38].

A pulse sequence is defined as the carefully designed combination of gradients, radiofrequency pulses, data sampling periods, and the time intervals between them. This sequence determines how the magnetization is manipulated, how the signals are collected, and how the spatial information is encoded to form the image [39].

Before delving deeper into MRI, it is essential to understand two key parameters: Repetition Time ($TR$) and Echo Time ($TE$), which are fundamental to image formation. $TR$ refers to the repetition time of the entire acquisition protocol, which is the interval between successive radiofrequency excitation pulses applied to a specific slice. This parameter directly influences the image contrast and the characteristics of the acquired signal. On the other hand, $TE$ is the interval between applying the radiofrequency pulse and detecting the echo signal, allowing the differentiation of tissues or materials based on relaxation parameters [40].

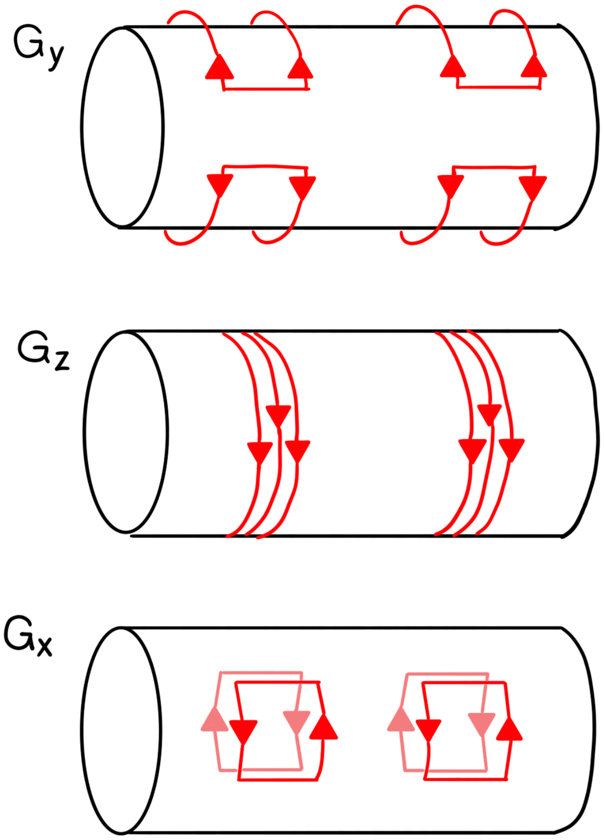

Figure 1.6: Illustration of the three gradient coils ($G_x$, $G_y$, and $G_z$) used in MRI. Each set of coils generates a magnetic field gradient along a specific spatial direction, allowing for spatial encoding of the MRI signal.

These two times are closely related to the relaxation times observed in NMR. When the $TR$ is long compared to $T_1$, the effects of $T_1$ relaxation become negligible. Similarly, if the $TE$ is short relative to $T_2$, the effects of $T_2$ relaxation are not significant.

### 1.4.1 Spacial Encoding

Spatial encoding is essential for obtaining meaningful images of a sample. This technique encompasses a series of processes carried out by MRI equipment to determine the origin of the signals within the sample. The main functions include slice selection, phase encoding, and frequency encoding [41].

The first step in spatial encoding is selecting the slice plane. A magnetic field gradient, known as the Slice Selection Gradient ($G_{SS}$), is applied perpendicular to the desired slice plane [42].

This gradient is added to $B_0$, causing a variation in the resonance frequency of the protons that is proportional to $G_{SS}$. Simultaneously, the system applies an RF pulse with a frequency corresponding to that of the protons located in the desired slice plane. This process alters the magnetization of only the protons in that plane, while hydrogen nuclei outside the slice remain inactive and do not produce signals. A selective pulse combines the RF pulse, slice selection gradient, and specific resonance frequency [43].

After selecting the plane, magnetic field gradients further stimulate the protons in the slice to encode their positions in the horizontal (frequency encoding) and vertical (phase encoding) directions. The gradient amplitude and RF pulse characteristics define both the thickness and the position of the slice.

The second step in spatial encoding involves applying a phase encoding gradient in the vertical direction. This gradient functions for a limited time, and while active, it modifies the resonance frequencies of the spins, causing a phase shift that remains even after the gradient is turned off. As a result, all protons precess at the same frequency but with different phases. Protons in the same line, perpendicular to the gradient direction, share the same phase. The system preserves the phase difference until it records the signal. This can be observed in the Figure [1.7].

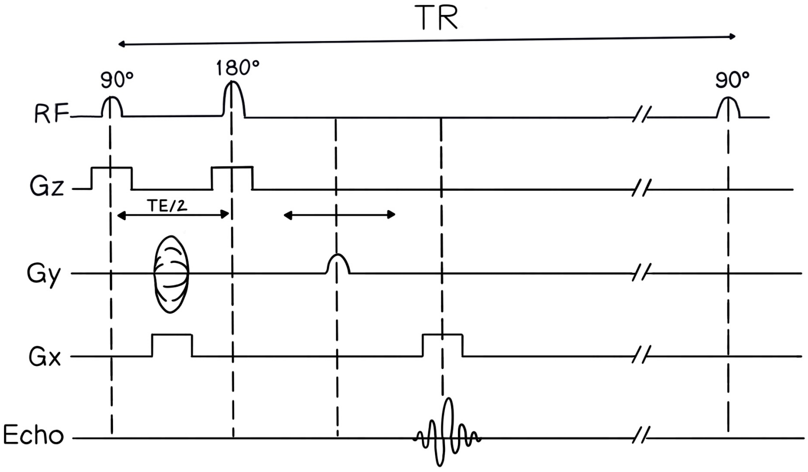

Figure 1.7: Diagram representing the spatial encoding steps in MRI. The RF pulses (90° and 180°) interact with the $G_x$, $G_y$, and $G_z$ gradients to achieve slice selection, phase encoding, and frequency encoding, respectively. The resulting echo signal is collected at the end of the sequence.

When the signal is received, each line of protons shows a slight phase shift, which is reflected in the emitted signals, making them slightly out of phase to varying degrees. To create an image, we must combine the different phase-shifted acquisitions, which are incrementally adjusted.

The final step in spatial encoding involves applying the frequency encoding gradient, which operates in the last direction (horizontal) when the signal is received. This gradient modifies the Larmor frequencies while active, creating columns of protons with identical frequencies.

We directly incorporate the frequency information into the acquired data by applying this gradient concurrently with signal reception. The duration of a 2D image sequence is given by the equation (1.10):

$$Duration = TR \times N_{Py} \times N_{ex}, \tag{1.10}$$

where $TR$ is the repetition time, $N_{Py}$ is the number of phase encoding steps, and $N_{ex}$ is the number of excitations.

The term "slice thickness" can also be referred to as "voxel," which indicates the volume of a three-dimensional pixel. These voxels are composed of pixel matrices, and the pixel size and the slice thickness determine their size. This factor can affect the quality of the generated image in various ways [44]. One way to calculate the pixel and voxel size of an image is by using the equations (1.11) and (1.12):

$$pixel\ size = \frac{FOV}{matrix} \times \frac{FOV}{matrix} \tag{1.11}$$

$$voxel\ size = \frac{FOV}{matrix} \times \frac{FOV}{matrix} \times slice\ thickness, \tag{1.12}$$

where another essential aspect that influences image quality is the field of view (FOV), which represents the total viewing angle of the scan. A larger FOV results in bigger voxels, which reduces resolution and image quality [45]. On the other hand, a smaller FOV provides higher resolution [3] and more detailed images.

### 1.4.2 Pulse Sequence

A pulse sequence is a set of radiofrequency pulses, and magnetic field gradients applied precisely to uniformize the intensity signal of all protons within a specific sample volume.

---

[3] Resolution is a crucial factor in image generation, as it refers to the ability to distinguish different structures within an image. It is determined by the number of pixels present within a specified FOV.

This process is crucial for generating images with particular characteristics, such as image quality, appearance, and acquisition speed [46].

In addition, it is possible to add a new excitation pulse to the sequences to manipulate the total magnetization of specific parts of the sample within an imaging volume [47]. The pulse sequence allows differentiation of these areas, affecting the contribution of the detected signal and, consequently, the image quality and contrast.

It is only possible to discuss pulse sequences by mentioning the most fundamental sequence in magnetic resonance, the spin echo. This sequence consists of applying an initial 90° pulse, followed by a 180° refocusing pulse, and finally, acquiring the generated signal.

When all the spins are aligned parallel to the magnetic field $B_0$, applying a 90° pulse causes these spins to align within the XY plane. Due to the magnetic field's inhomogeneity, the total magnetic moment begins to progress, leading to signal decay. A 180° pulse is applied to correct this effect, allowing the magnetic moments to refocus. This process restores the total moment and initiates the formation of the echo signal [48].

At the moment of complete refocusing, the $T_2$ signal can be measured. After repeating this process multiple times and forming several echoes, it becomes possible to eliminate the effects of $T_2^*$. Meanwhile, as the spins gradually return to their equilibrium position, aligning with the $B_0$ field, $T_1$ relaxation takes place.

The spin echo was the first pulse sequence used in magnetic resonance imaging, serving as the foundation for all subsequent sequences, which became known as contrast sequences. By carefully selecting the $TR$ and $TE$ parameters, it is possible to generate images with specific contrasts, such as those weighted in $T_1$, $T_2$, or proton density [49].

$T_1$-weighted images typically use short $TR$ and $TE$ values, while $T_2$-weighted images require a long $TR$ and an extended $TE$. Proton density is highlighted with a long $TR$ and a short $TE$. Based on these principles, a versatile and efficient technique was developed to accelerate image acquisition, producing $T_1$-, $T_2$-, and proton density-weighted images, known as RARE (Rapid Acquisition with Relaxation Enhancement) [50].

If we use the Spin Echo sequence and generate a sequence of multiple echoes instead of a single echo, we obtain the Carr-Purcell-Meiboom-Gill (CPMG) sequence (Figure [1.8]). This sequence is beneficial for studying porous materials, allowing for a more complete and efficient analysis of the $T_2$ relaxation time. Based on the same structure as the Spin Echo, the CPMG sequence collects echoes repetitively, enabling a more detailed investigation of the material's relaxation behavior [51].

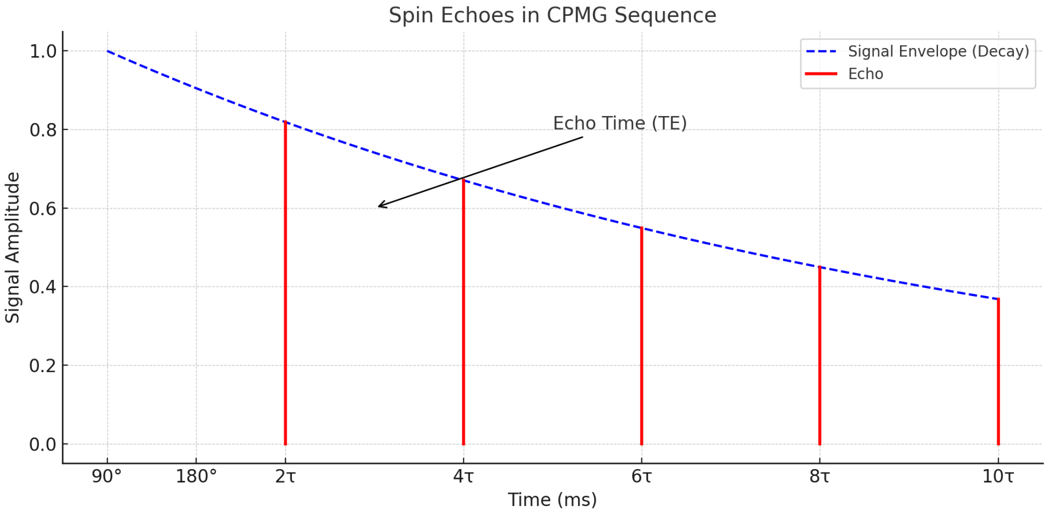

Figure 1.8: Representation of the CPMG sequence. The red vertical lines indicate spin echoes generated at specific TE, while the blue dashed line represents the decay envelope of the signal due to $T_2$ relaxation.

# Chapter 2

# Petrophysics

Petrophysics is a field dedicated to studying the physical properties of rocks and their interactions with fluids, which can include gases, liquids, hydrocarbons, or aqueous solutions. One of the primary applications of this field is in the petroleum industry, where there is significant interest in understanding the physical characteristics of rock formations that contain oil reservoirs [52].

A primary focus of this study is investigating the pore structure of rocks, which controls the accumulation and migration of hydrocarbons. Petrophysicists use systematic methodologies, including detailed workflows and well-log interpretation, to understand reservoirs' mineralogical and structural properties [53].

Although much of the research in petrophysics was originally directed toward the hydrocarbon industry, the field also encompasses applications in mining, water reservoirs, geothermal energy, and carbon capture and storage, contributing to global environmental and energy challenges [54].

## 2.1 Fundamental Petrophysical Properties

This field focuses on understanding the fluid properties on complex rock associated with petroleum reservoirs. It is essential to consider some fundamental petrophysical properties used in characterizing these reservoirs, such as porosity, permeability, lithology, water saturation, capillary pressure, and wettability [55].

All these petrophysical properties of a rock, such as porosity, permeability, saturation, and mineralogical composition, play a fundamental role in the interpretation of nuclear magnetic resonance data. They directly influence the relaxation times $T_1$ and $T_2$, as well as the response of the signals emitted by the analyzed material [56].

### 2.1.1 Lithology

Lithology is a branch of geology dedicated to studying rocks' composition, formation, and distribution on the Earth's surface. Its primary focus is the detailed description of rock characteristics such as color, texture, structure, mineralogical composition, and grain size. Additionally, lithology involves the analysis of lithification processes—the transformation of sediments into solid rocks—and the geological periods during which these processes occurred, contributing to understanding the planet's geological history [57].

### 2.1.2 Porosity

Reservoir rocks, such as sandstones and limestones, are typically formed by sand grains and carbonate particles. Due to the irregular shapes of these grains, they never fit perfectly together. The spaces between the grains, known as pores or interstices, are filled with fluids [58].

The porosity of reservoir rocks is defined as the fraction of the reservoir's total volume (bulk volume) that is not occupied by the rock [59]. The following equation (2.1) can express this property:

$$\phi = \frac{V_b - V_{gr}}{V_b} = \frac{V_p}{V_b}, \tag{2.1}$$

where $\phi$ is the porosity, $V_b$ is the bulk volume of the rock, $V_{gr}$ is the grain volume, and $V_p$ is the pore volume. This definition allows for quantifying the fluid storage capacity in the pores of a rock.

A porous rock can exhibit a wide range of porosity values. However, most sedimentary rocks have a porosity below 70% [60]. In contrast, oil reservoir rocks typically have an average porosity of 5% to 35%.

### 2.1.3 Permeability

When dealing with porous materials, it is essential to consider a rock reservoir's ability to allow fluids, such as water or hydrocarbons, to flow through its interconnected pores. This ability, called permeability, depends on the time and pressure applied [61].

The permeability of a rock is related to its porosity and to the size, packing, and distribution of the grains, as well as the degree of consolidation and cementation [62].

A widely used equation to measure the hydraulic permeability of a porous medium is Darcy's Law, which is expressed as follows in equation (2.2):

$$Q = \frac{kA\Delta P}{\mu L}, \tag{2.2}$$

where $Q$ is the volumetric flow rate of the fluid, $k$ is the permeability of the rock, $A$ is the cross-sectional area, $\Delta P$ is the pressure difference applied, $\mu$ is the fluid viscosity, and $L$ is the length of the sample.

### 2.1.4 Water Saturation

Water saturation ($S_w$) is a key property in reservoir characterization, as it directly impacts the assessment of recoverable hydrocarbon volumes and production planning operations [58].

This assessment involves estimating the volume of water present in the pore space, i.e., the fraction of the pore space occupied by water. The precise determination of $S_w$ is essential for calculating the amount of hydrocarbons in the reservoir and guiding efficient extraction strategies [63].

### 2.1.5 Wettability

When discussing two fluids in a porous medium, an important factor is understanding their relative adhesion to a solid surface, known as wettability.

Wettability determines each fluid's tendency to spread or adhere to the rock surface in a porous material with two immiscible liquids [64].

In a rock sample with two fluids, such as water and oil, water tends to occupy the smaller pores, wetting most of the surfaces of these larger pores. On the other hand, oil will rest on a layer of water that spreads over the rock surface [65].

When the rock surface is preferentially water-wet, water will be absorbed (imbibed) into the smaller pores, while the oil will remain in the central part or the larger pores. When the system comes into contact with water, the oil will be displaced from the core, as water has a greater affinity for the rock surfaces, causing the displacement of the oil [66].

### 2.1.6 Capillary Pressure

Capillary pressure is the pressure difference between two immiscible fluids in a porous medium caused by the interfacial tension between them. It depends on the average size of the capillaries and the interfacial tensions. Capillary pressure is crucial in porous media as it controls fluid flow through them [67].

For example, in a water-wet sample, the walls of the capillaries are coated with a thin film of the wetting fluid, while the oil, which is the non-wetting fluid, rests on this film. In this case, the pressure in the non-wetting fluid is higher than in the wetting fluid. As a result, the interface between the fluids exhibits a convex curvature relative to the non-wetting fluid.

Understanding the capillary pressure of a porous medium allows for various experiments on samples, such as mercury injection under high pressure. This method, known as mercury intrusion porosimetry, provides insights into the sample's pore size distribution.

During the experiment, mercury, a non-wetting fluid, is forced to penetrate the sample's pores as pressure increases. The relationship between the applied pressure and the volume of intruded mercury provides detailed information about the pores' distribution and size. This technique is widely used in reservoir rock characterization studies, ceramic materials, and other porous media and is essential for evaluating porosity and permeability [68].

## 2.2 Fluid-Rock Interation

Fluid-rock interaction is the process by which fluids and rocks chemically and physically react, altering the rocks' properties. This process occurs in various parts of the Earth, especially in regions where aqueous solutions are present, and can influence a range of important aspects [69].

Firstly, the fluid-rock interaction can affect rocks' properties in several ways. Notable among these are changes in wettability, solubility, diffusivity, and adsorption, which directly impact rocks' behavior in natural or engineering environments.

Additionally, the fluid-rock interaction is closely related to changes in mineral phases. The primary mechanism of this interaction is the dissolution and precipitation of mineral phases, which can alter the mineralogical composition of rocks, affecting their structure and mechanical behavior. This phenomenon is crucial in forming new minerals in weathering environments, such as mineralization processes and geothermal systems [70].

The fluid-rock interaction can also significantly impact rock strength. The presence of fluids, particularly under extreme pressure and temperature conditions, can reduce rock strength, facilitating their fracture or disintegration. This is especially relevant in areas such as petroleum and gas reservoir engineering, where controlling rock strength is critical for extraction efficiency [71].

In summary, fluid-rock interaction is a complex process that affects various aspects of rock behavior, from their physical and mechanical properties to their seismic response. A detailed study of this process is essential for advancements in natural resource exploration, geotechnical engineering, and understanding large-scale geological phenomena.

# Chapter 3

# Results

This work was carefully structured to ensure a thorough analysis of porous rock samples and their interaction with fluids. The experimental approach followed three main stages, allowing the creation, saturation, and subsequent evaluation of the samples using advanced NMR techniques.

The methodology was divided into three steps: sintering the porous rocks, saturation of the samples with water and oil, and analysis of these samples through NMR. These procedures enabled the precise development of the samples and a detailed understanding of their behavior, including the dynamics of fluids within the pores and their quantification.

The foundation for developing this methodology was based on the master's dissertation of Dr. Bruno Chencarek [72]. This dissertation provided essential insights for creating the current method, from the sintering process of silica porous rocks with different grain sizes to the saturation procedure.

## 3.1 Sintering of the Samples

For the initial process, soda-lime glass microspheres (composed of silica, lime, and carbonate) produced by the company Multiesferas were selected for the sintering of the rocks, with three distinct granulometry ranges chosen. The main reason for selecting this material was its abundance and familiar presence in rocks from the continental crust, especially in underwater rocks of oil reservoirs. These reservoirs are predominantly composed of sedimentary rocks, whose chemical composition is mainly based on silica [73]. Additionally, the low cost of the microspheres, obtained from recycled glass used in sandblasting activities, was another factor in this choice.

The samples were sieved to define three granulometry intervals: Granulation 1 (G1), from 75 to 125 $m$; Granulation 2 (G2), from 150 to 212 $m$; and Granulation 3 (G3), from 250 to 300 $m$. These ranges were selected to enable the analysis of the saturation process and porosity in different grain sizes, providing a comprehensive understanding of fluid behavior in pores of varying sizes. We used sieves from the company *Jomon Cerâmicas Avançadas*, requiring two sizes for each granulometry range. For G1, we used sieves of 75 $m$ and 125 $m$; for G2, we used sieves of 150 $m$ and 212 $m$; and for G3, we used sieves of 250 $m$ and 300 $m$.

For the sintering process of the rocks, the soda-lime microspheres were placed into high-alumina-based ceramic molds, known as crucibles, with diameters of 7.5 $mm$ and lengths of 38 $mm$, respectively, which were specifically made to meet the reference dimensions of the samples used in the NMR equipment, at the Figure [3.1].

Figure 3.1: High alumina-based ceramic cylindrical molds with diameters of 7.5 $mm$ and lengths of 38 $mm$, respectively, used for sample preparation in experimental procedures.

The goal was to obtain a porous rock capable of being saturated with two different fluids. It was necessary to understand the appropriate thermal ramps for each granulometry range, respecting their chemical properties. The challenge was to promote partial sintering of the grains, meaning to find a thermal ramp that would bond the grains without fully melting them, thereby preserving the degree of porosity during the sintering process and enabling fluid saturation.

To create the appropriate thermal ramp, it was essential to understand the annealing properties, which involve a heat treatment to alter the material's microstructure and modify its properties. This process consists of controlled heating in a furnace to a specific temperature, followed by slow cooling [74]. Additionally, it was necessary to consider the limitations of the furnace used, a Carbolite CWF 1300, with a maximum temperature of 1300°C and a heating rate of 7°C per minute [75]. With these parameters in mind, we had to develop a thermal ramp that respected the material's properties and the equipment's capabilities [76].

The first granulometry required more care and delicacy due to the small size of its grains. During the interval between the plateaus, the annealing process took place, making it essential to have enough time on the plateaus and between them for the sintering to occur without fusing the pores. For this reason, both plateaus were maintained for the minimum time necessary for this process, as described in Table [3.1] and the Figure [3.2] below:

| **GRANULATION 1** | | |
|---|---|---|
| **Time (min)** | **Temperature (°C)** | **Thermal Rate (°C/min)** |
| 0 - 107 | 40 - 560 | 5 |
| 108 - 113 | 560 | 0 |
| 114 - 140 | 560 - 700 | 5 |
| 141 - 147 | 700 | 0 |
| 148 - 826 | 700 - 40 | 1 |
| 827 | 40 | 0 |

Table 3.1: Thermal ramp parameters for Granulation 1 (G1), showing the time intervals, temperature variations, and thermal rates applied during the process.

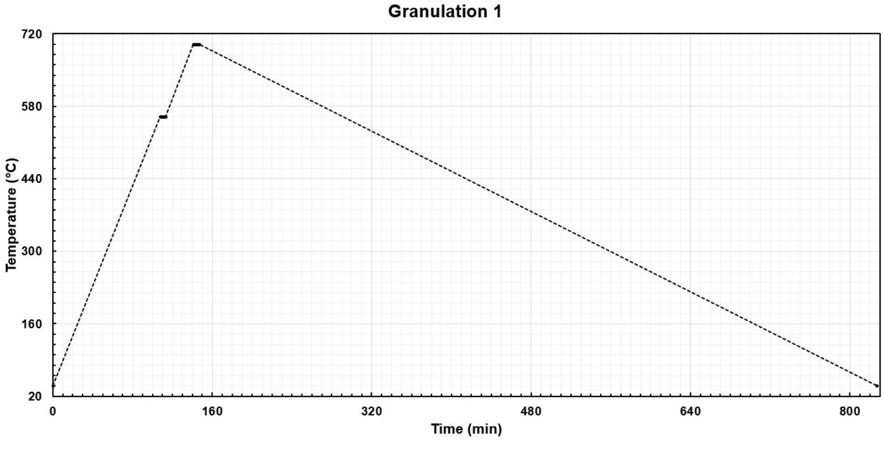

Figure 3.2: Temperature profile of Granulation 1 (G1), illustrating the thermal ramp process over time.

Thus, the second granulometry was based on the knowledge gained from the ramp of the previous granulometry [3.2], gradually adding more time to the second plateau to achieve partial sintering. Set the total time of the ramp to 5 minutes on the first plateau and 8 minutes on the second plateau, as presented in table [3.2] and the graph [3.3] below:

| **GRANULATION 2** | | |
|---|---|---|
| **Time (min)** | **Temperature (°C)** | **Thermal Rate (°C/min)** |
| 0 - 107 | 40 - 560 | 5 |
| 108 - 113 | 560 | 0 |
| 114 - 140 | 560 - 700 | 5 |
| 141 - 149 | 700 | 0 |
| 150 - 828 | 700 - 40 | 1 |
| 829 | 40 | 0 |

Table 3.2: Thermal ramp parameters for Granulation 2 (G2), showing the time intervals, temperature variations, and thermal rates applied during the process.

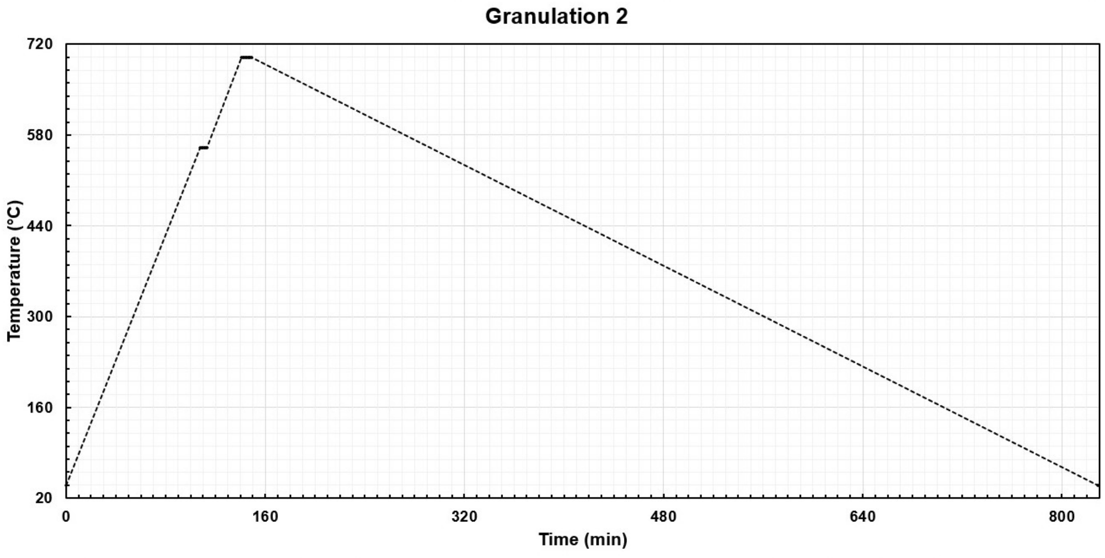

Figure 3.3: Temperature profile of Granulation 2 (G2), illustrating the thermal ramp process over time.

Based on the previous two granulometries [3.2][3.3], was observed a systematic pattern between the plateau time and the increase in granulometry. For the largest granulometry, was added 2 minutes to the second plateau, resulting in 5 minutes on the first plateau and 10 minutes on the second, as illustrated in the Figure [3.4] and the Table [3.3] below:

| **GRANULATION 3** | | |
|---|---|---|
| **Time (min)** | **Temperature (°C)** | **Thermal Rate (°C/min)** |
| 0 - 107 | 40 - 560 | 5 |
| 108 - 113 | 560 | 0 |
| 114 - 140 | 560 - 700 | 5 |
| 141 - 151 | 700 | 0 |
| 152 - 830 | 700 - 40 | 1 |
| 831 | 40 | 0 |

Table 3.3: Thermal ramp parameters for Granulation 3 (G3), showing the time intervals, temperature variations, and thermal rates applied during the process.

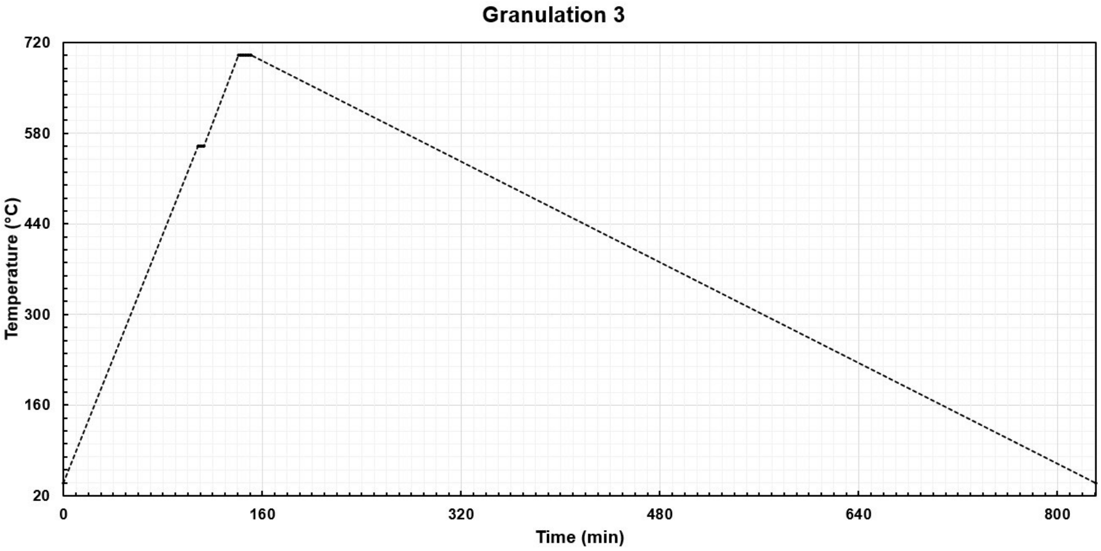

Figure 3.4: Temperature profile of Granulation 3 (G3), illustrating the thermal ramp process over time.

After adjusting the thermal ramps for the three different granulometries, was obtained the samples illustrated in Figures (3.5; 3.6; 3.7). The samples were subjected to scanning electron microscopy (SEM) analysis to evaluate the effectiveness of the thermal treatment process. This analysis allowed me to confirm the microstructure's expected characteristics after adjusting the thermal ramps, enabling the validation of the parameters applied in the process.

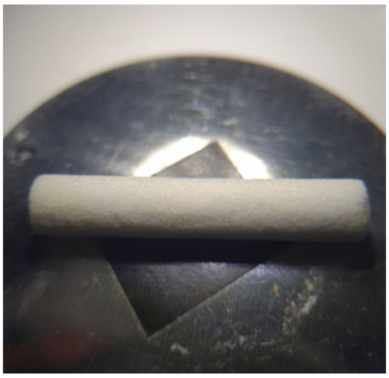

Figure 3.5: Finished sample of Granulation 1 (cylindrical shape).

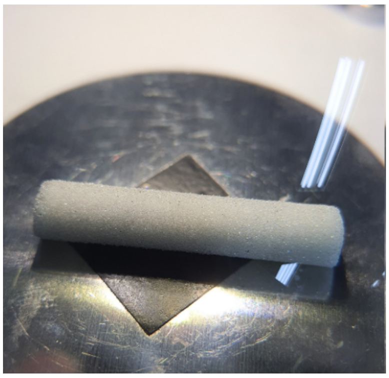

Figure 3.6: Finished sample of Granulation 2 (cylindrical shape).

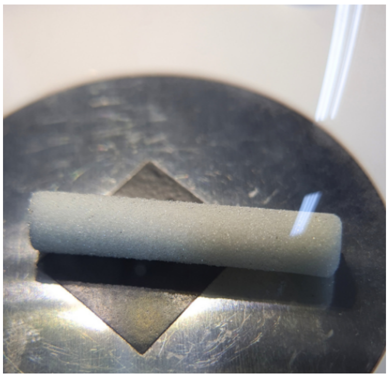

Figure 3.7: Finished sample of Granulation 3 (cylindrical shape).

## 3.2 Characterization of the Samples

The samples were characterized using a scanning electron microscope (SEM) with the JEOL JSM-6490 equipment at the LabNANO Laboratory of CBPF. This process allowed for the analysis of the effect of thermal treatment on the sintering of the grains in each sample. It was first necessary to metallize the samples with a gold layer using the metallizer EMITECH K550X, which utilizes Argon 5 PSI, to generate the SEM images. The deposition process took about 4 minutes, resulting in a layer approximately 5 *nm* thick, which is necessary to ensure high-quality image analysis.

The thermal ramps described earlier ([3.1]; [3.2]; [3.3]) show partial sintering in all granulometries, confirming that the ramps used were suitable for the process. Below are the electron microscope images ([3.8]; [3.9]; [3.10]) with the respective parameters used in the Table [3.4]:

| **SEM PARAMETER** | | | |
|---|---|---|---|
| **Parameter** | **1st image** | **2nd image** | **3rd image** |
| **Acc. Volt (kV)** | 10 | 10 | 10 |
| **Spotsize** | 50 | 50 | 44 |
| **WD (mm)** | 15 | 15 | 15 |
| **Magnification** | 25 | 50 | 95 |

Table 3.4: Parameters used for acquiring SEM images, including accelerating voltage, spot size, working distance (WD), and magnification for three different images.

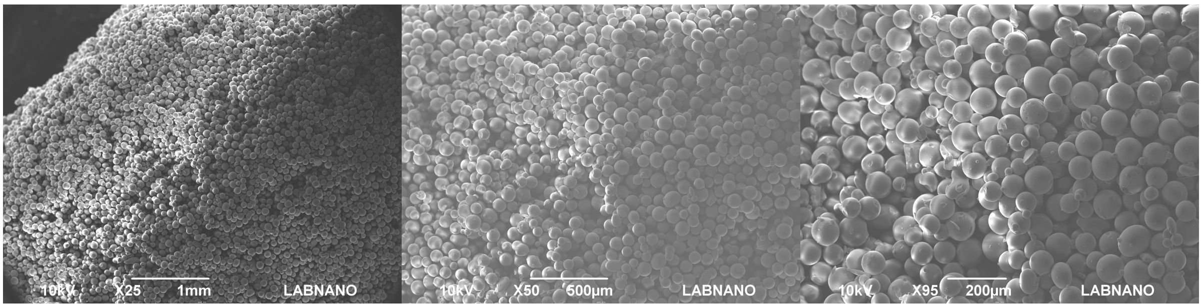

Figure 3.8: Electron microscope image showing the grain morphology of samples G1 at different magnifications.

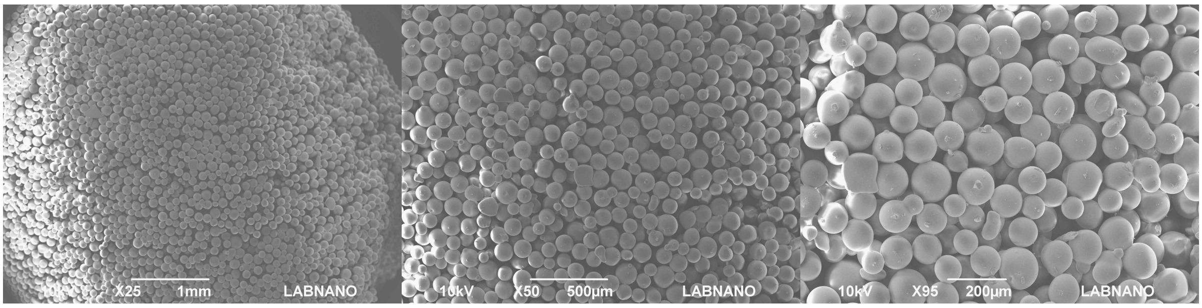

Figure 3.9: Electron microscope image showing the grain morphology of samples G2 at different magnifications.

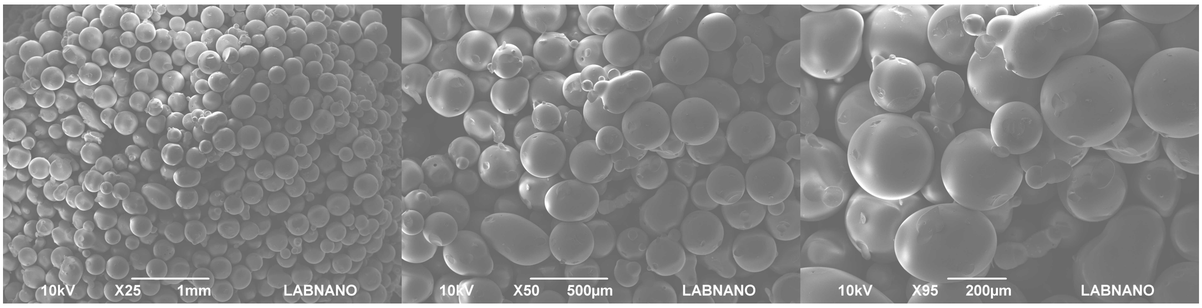

Figure 3.10: Electron microscope image showing the grain morphology of samples G3 at different magnifications.

With these images, it is possible to observe that the defined ramps are achieving the main objective: partial sintering of the grains while preserving the necessary pore spaces for saturation. However, the electron microscope equipment was essential in identifying the correct ramps, allowing for the analysis of how excessive time on the plateaus led to the unwanted fusion of grains, which needed to be avoided. Below are the electron microscope images ([3.11]; [3.9]; [3.10]) showing how the grains fused due to prolonged time on the plateaus.

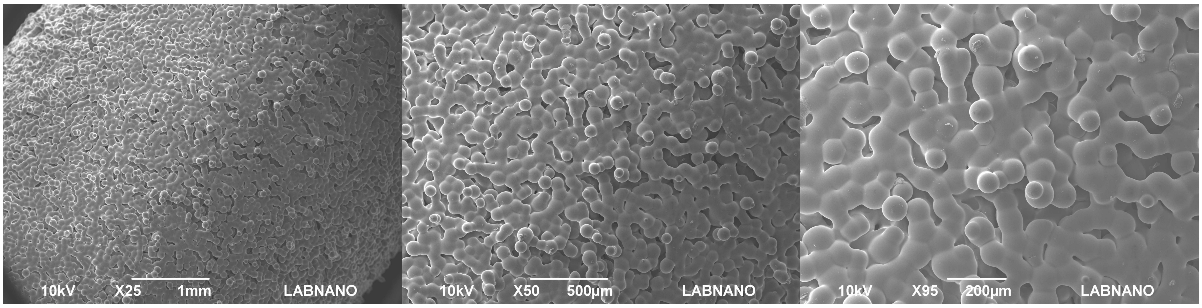

Figure 3.11: Electron microscope images showing the fused grains of Sample G1 at different magnifications.

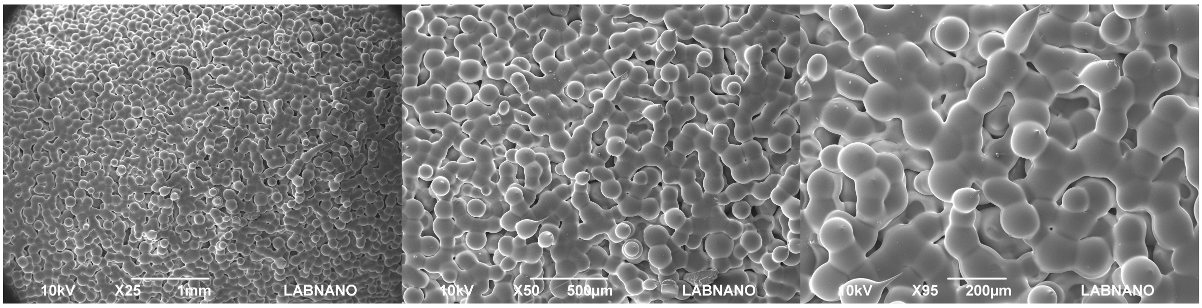

Figure 3.12: Electron microscope images showing the fused grains of Sample G2 at different magnifications.

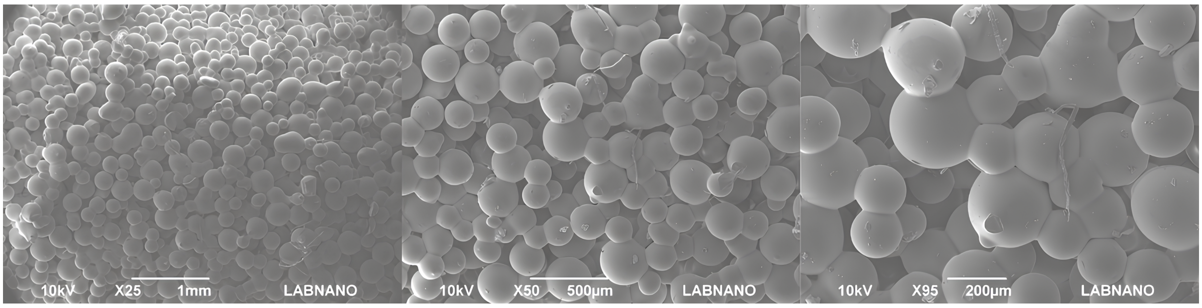

Figure 3.13: Electron microscope images showing the fused grains of Sample G3 at different magnifications.

## 3.3 Saturation of the Samples

The saturation process in porous rocks, similar to what occurs in oil reservoirs, follows the model described by Ahmed (2010) [77], where pores initially filled with water are progressively invaded by oil during the injection of fluids under pressure. The primary objective of this stage was to replicate the environment of underwater oil reservoirs, simulating the initial phase of the extraction process. In the early stage, the pores of the rocks are filled with water, and over time, oil is injected into these rocks under pressure, displacing some of the water present [7].

For this reason, the saturation stage of the samples was conducted carefully to ensure accurate results in the MRI analysis. Before saturation with water, all necessary measurements were taken, including the dry weight of the sample, its height, and diameter. The sample was then placed in a vacuum system, along with a beaker containing water. This equipment can be seen in the images ([3.14]; [3.15]). The vacuum was applied for 40 minutes, reaching a pressure of -640 $mmHg$, at which point the sample was submerged in the beaker of distilled water and remained under vacuum for an additional hour. After this period, the sample was removed from the equipment and weighed again to calculate the water that filled the pores. This measurement was termed the wet mass of the sample.

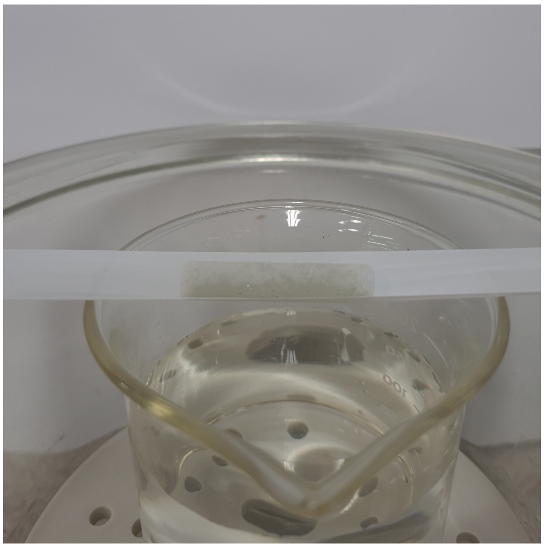

Figure 3.14: Open vacuum desiccator with a beaker containing distilled water.

Figure 3.15: Closed vacuum desiccator with an attached hose.

After saturation with water, it is necessary to inject oil into the sample in a controlled manner. The oil used in this process is EMCA oil, derived from petroleum, with characteristics similar to those required for the analysis [78]. For this procedure, a low-cost device was developed, inspired by the concept of a commercial saturator that injects oil into the sample consistently and in a controlled manner.

The proposed solution uses a 10 $ml$ hospital syringe from the PROCARE brand, connected to a rubber hose that keeps the sample stable during the injection and ensures the separation between the oil and the water extracted from the sample, preventing the mixing of the fluids. This system allows for precise control of the oil addition, as illustrated in the images ([3.16]; [3.17]) below.

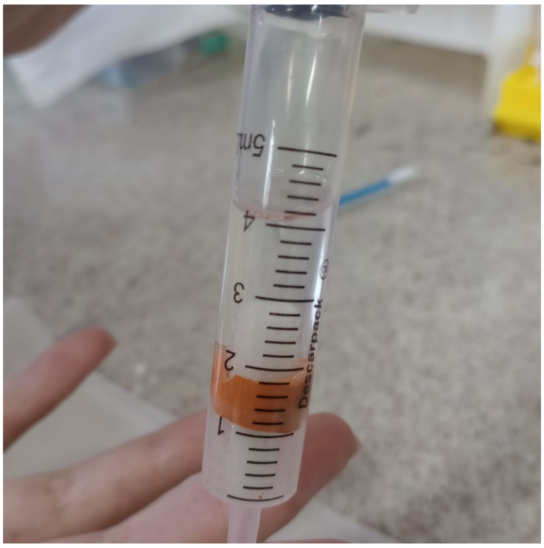

Figure 3.16: Syringe containing oil for sample saturation.

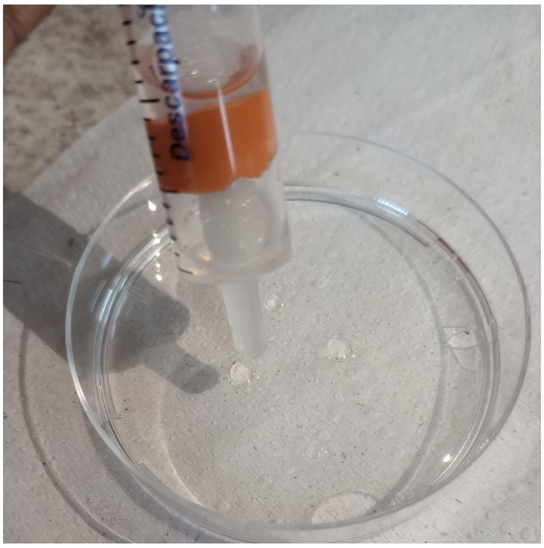

Figure 3.17: Outcome of the saturation process with both fluids present.

Despite the innovative idea for the low-cost saturator, some modifications were still necessary because the rubber hose could not prevent oil leakage, causing it to mix with the water expelled from the sample. This prevented the precise measurement of the amount of water displaced about the volume of oil injected. For this reason, a new design was developed in collaboration with the Laboratory of Instrumentation and Mechanical Technology (LITMec), creating a piece that fit the exact size of the sample and syringe. This piece ensured the containment of the oil, allowing only the water to be expelled from the sample during the oil injection.

Based on the observed needs, a specific sample holder for the synthetic rocks was designed and made from aluminum. The saturator used an elastic ring (ERING) between the sample holder and the porous rock to ensure an effective seal, preventing any oil leakage that could compromise the precise measurement of the displaced water. The developed parts are illustrated in the images ([3.18]; [3.19]; [3.20]) below.

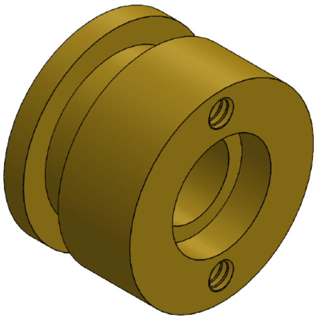

Figure 3.18: Sample holder.

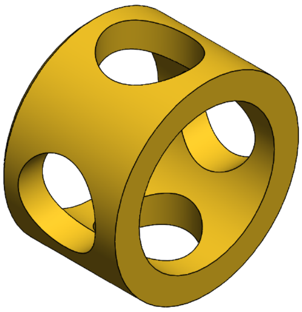

Figure 3.19: Viewing spacer.

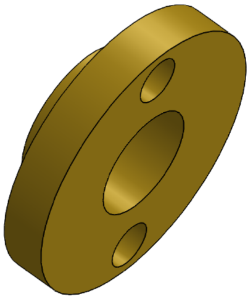

Figure 3.20: Overlaid.

Implementing this sample holder resulted in excellent saturation tests. The controlled injection of oil into the sample was accompanied by simultaneous water removal, maintaining the exact amount and preventing mixing between the two fluids at the end of the process. This setup led to a highly efficient, low-cost saturator that ensured precise oil saturation of the sample.

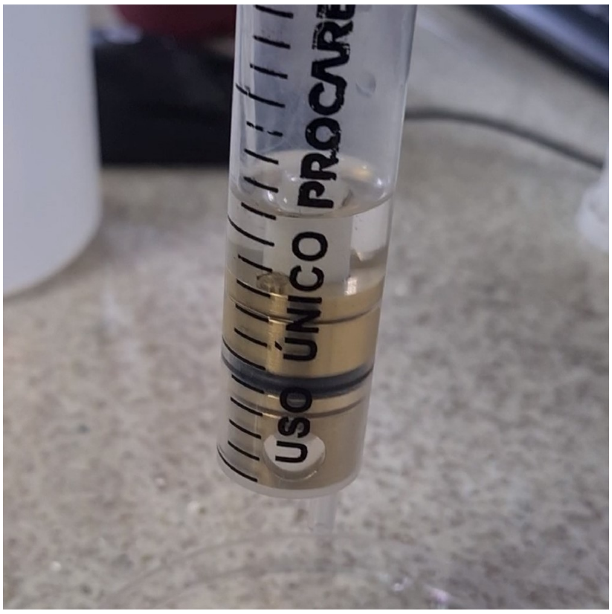

Figure 3.21: Finalized low-cost saturator with components developed by LITMec.

With the final saturator completed (Figure [3.21]) and its efficiency proven, the sample saturation process began, aiming for image analysis by nuclear magnetic resonance. It was necessary to control the sample information strictly to determine the amount of oil and water present accurately. The sample, identified as AMS54, was selected with granulometry 3. Using a caliper, the height (38 $mm$) and diameter (7.5 $mm$) measurements were recorded, and with a high-precision balance, the dry mass of the sample was obtained as 2.57 $g$. The first saturation stage began with these data: the sample was placed in the vacuum compartment and then submerged in water.

After complete saturation with water, the wet mass of the sample was recorded as 3.12 $g$, indicating an initial water volume of 0.55 $ml$. The sample was then inserted into the saturating syringe containing 1 $ml$ of oil. Notably, the amount of oil inserted into the sample corresponded to approximately 11% of the volume initially placed in the saturator, resulting in a final proportion of 0.44 $ml$ of water and 0.11 $ml$ of oil. With these values, it was possible to calculate the presence of 20% oil and 80% water in the sample, with a total porosity of 67%. All of this information is shown in the Table [3.5].

| **Parameters** | **AMS 54** | **Parameters** | **AMS 54** |
|---|---|---|---|
| Dry Mass | 2.57 g | Oil that Entered | 11% |
| Wet Mass | 3.12 g | Final Oil Volume | 0.11 ml |
| Diameter | 0.74 cm | Final Water Volume | 0.44 ml |
| Height | 3.12 cm | Initial Water Volume | 0.55 ml |
| Porosity | 67% | Water AMS | 80% |
| Initial Oil Volume | 1 ml | Oil AMS | 20% |

Table 3.5: Fluid saturation parameters of sample AMS 54, including mass, dimensions, porosity, and fluid distribution before and after saturation.

After collecting this information, the sample is wrapped in Teflon tape to minimize liquid loss during the image analysis using NMR equipment. Teflon is the choice of material because it does not interfere with the image acquisition. Once the sample is prepared, the image analysis process begins. This allows for the precise quantification of the fluids present through a single image analysis program, ensuring the results' reliability.

With the methodology established and the sintering and saturation processes of the samples completed, the analysis of the images of these samples began using the high-field NMR equipment, a Bruker 500 $MHz$, at the CBPF Nuclear Magnetic Resonance Laboratory (Figure [3.22]). This phase aimed to examine the entire sample structure, integrating the information obtained during the saturation process with the equipment-generated data.

Figure 3.22: High-field Nuclear Magnetic Resonance equipment, Bruker 500 $MHz$, used at the CBPF Nuclear Magnetic Resonance Laboratory analysis of saturated samples.

The primary goal of this phase was to develop an effective method to quantify the fluids present in the samples. Several approaches were employed to achieve this objective: chemical shift contrast, spectral analysis of rock and bulk samples, $T_1$ and $T_2$ relaxation, and image analysis methods. Each of these techniques played a crucial role in validating the fluid quantification program for the sample. In parallel, the information obtained during the saturation process served as a comparison parameter with the values generated by the program, allowing for an accurate evaluation of the method's efficiency.

## 3.4 Chemical Shift Contrast

To understand the behavior of samples within the NMR equipment, a spectral study was conducted on three samples of synthetic porous rocks, all with the same granulation (G3) but saturated in different ways. One sample was saturated exclusively with water, another only with oil, and the last with both fluids, known as AMS54. Is possible to find more the detailed information about this sample in Section [3.5]. The Figure [3.23] presents the spectra obtained for each to compare the behavior of these three sample variations.

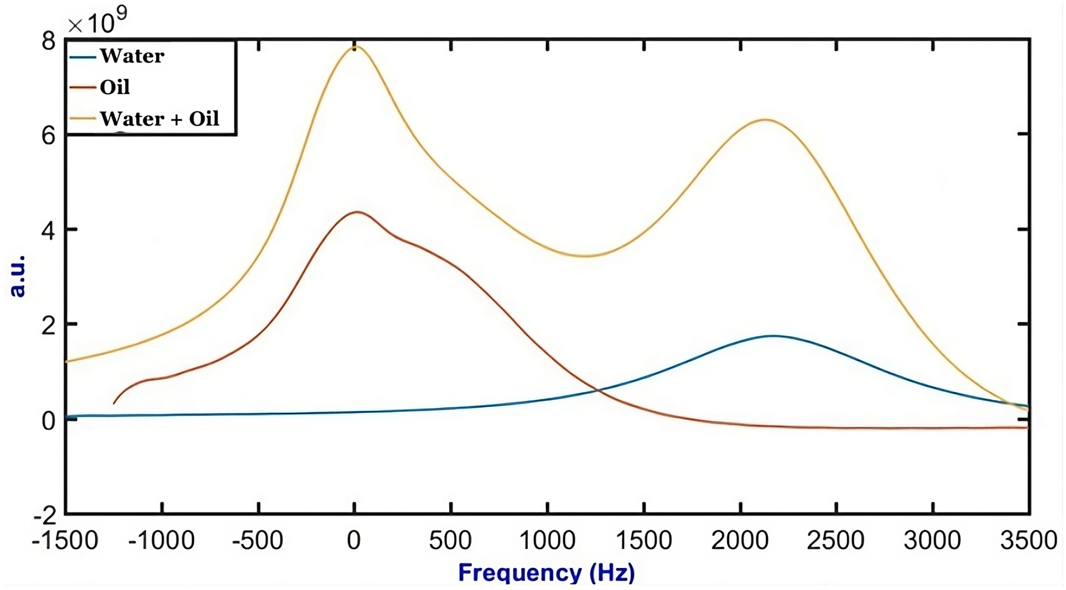

Figure 3.23: NMR spectra of fluids in synthetic porous rock samples. The curves represent the signals corresponding to water (blue), oil (red), and their mixture (yellow), highlighting the differences in spectral responses as a function of frequency.

According to the legend in Figure [3.23], the yellow spectrum represents the AMS54 sample, saturated with both fluids, while the red spectrum corresponds to the sample saturated exclusively with oil, and the blue spectrum represents the sample saturated only with water. Analyzing these spectra allowed for identifying specific peaks for each fluid, facilitating an understanding of their individual and combined behaviors. By observing exclusively the yellow spectrum, it is possible to distinguish that the first peak corresponds to oil and the second to water. This distinction enabled the use of a technique known as chemical shift contrast.

This technique is widely used in magnetic resonance imaging to allow the simultaneous localization of spectra from multiple components, taking advantage of the difference in proton resonance frequencies, which can cause variations in signal intensity. It is based on a pulse sequence, which helps confirming the presence of lipids (oil) and water through the difference in resonance frequencies [79].

In simpler terms, identifying intensity signals in the spectra using a specific bandwidth for the fluids enables visual separation of the fluids in the image. Figure [3.24] illustrates the result of this technique.

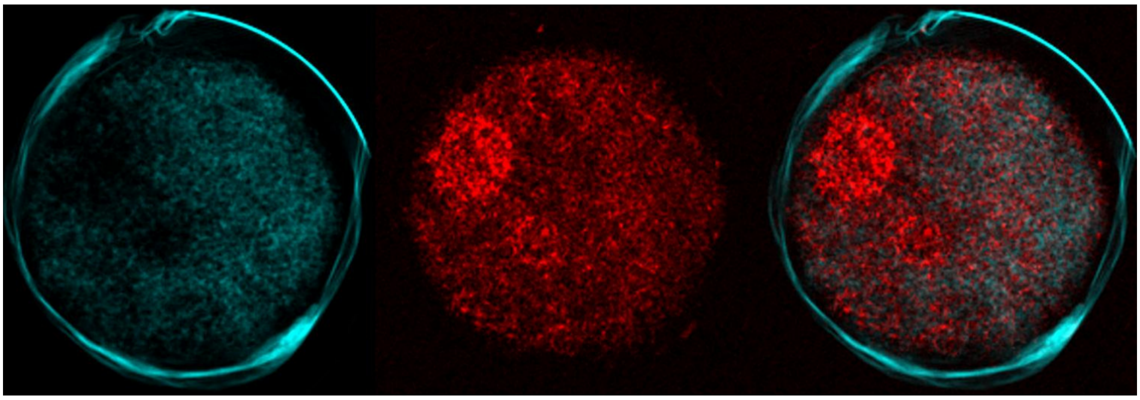

Figure 3.24: Visualization of a rock sample saturated with fluids using chemical contrast. (A) Blue pixels represent oil distribution, (B) Red pixels indicate water presence, and (C) The combined image shows the spatial distribution of both fluids within the sample.

In Figure [3.24], we see the AMS54 sample, where the fluids were artificially colored: water in shades of red and oil in shades of blue. The chemical shift contrast technique proved effective in synthetic rock samples with controlled porosity and fluids, allowing both the separation and, possibility of quantification of the fluids present using this approach.

However, in real rocks, significant challenges arise. A critical factor in this process is the overlap of the spectral lines of the fluids, which prevents the precise separation of intensities and consequently results in the loss of detailed information. This problem is common to natural rocks, as it was also observed in samples with smaller granulation, such as G2. However, the effect became more noticeable and problematic in samples with smaller granulation, for example, the G1, making it impossible to use them for efficient fluid quantification.

Figure [3.25] illustrates this limitation, comparing the spectrum of a bulk water and oil sample with that of a synthetic porous rock sample. It highlights the broadening and overlap of the spectral lines, emphasizing that, in real rocks, this approach would not be practical due to the interference between the fluid signals.

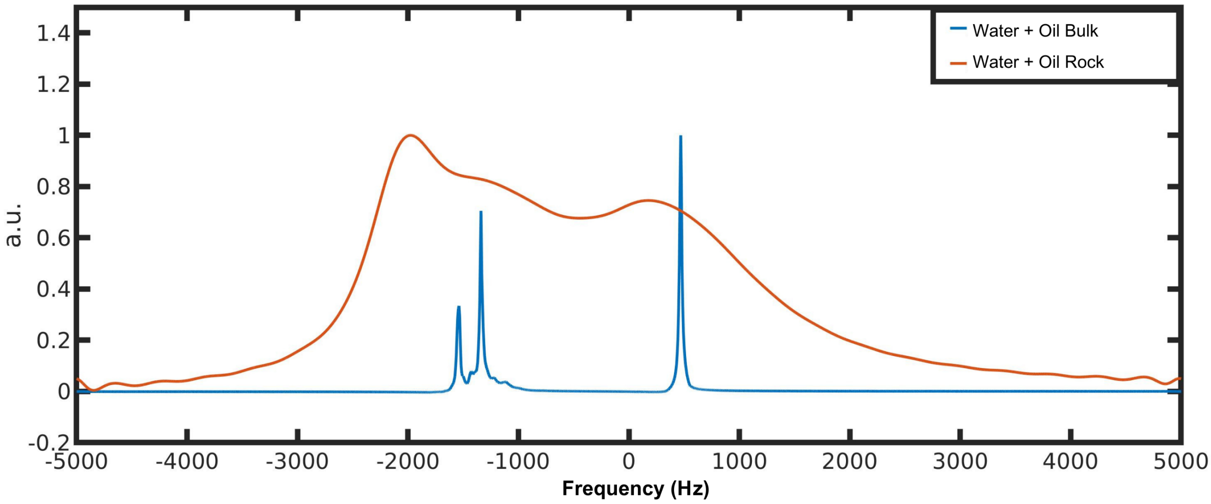

Figure 3.25: NMR spectrum for a water and oil mixture in a porous medium (rock) and in bulk form. A significant broadening of the spectral lines is observed in the porous medium (orange curve) compared to the bulk sample (blue curve), indicating greater interaction between the fluids and the rock matrix, resulting in shorter relaxation times and frequency dispersion.

Although this approach proved effective for some samples, its application in the real world would not be feasible, leading to the search for other contrast methods to quantify the fluids within these rocks. However, the chemical shift contrast technique was essential for identifying the fluids through the spectra, providing a crucial initial analysis for the study.

## 3.5 Relaxation Contrast

These limitations have driven the search for alternative methods for fluid quantification. Initially, we characterized the behavior of isolated fluids, both in the bulk state and in porous media. As discussed in Section 1.2 of Chapter 1, regarding $T_1$ relaxation, we observed significant variations in the relaxation times of water and oil. This difference is clearly illustrated in the Figure [3.26], which depicts the relaxation of these two fluids within a rock sample.

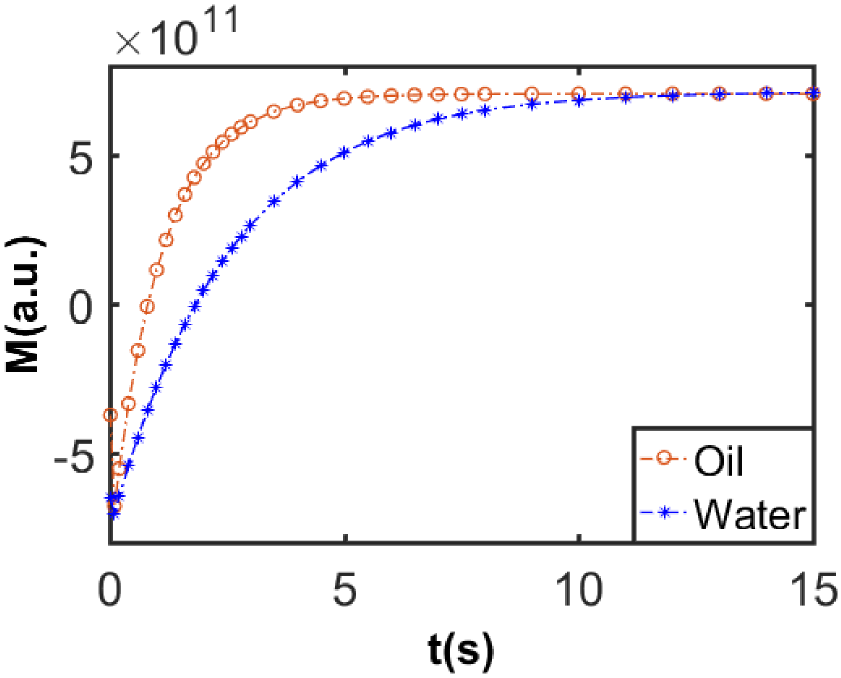

Figure 3.26: $T_1$ relaxation curves for water (blue) and oil (orange) within the rock. The observed relaxation times are approximately 2.1 $s$ for water and 0.5 $s$ for oil.

The $T_1$ relaxation is related to the size and movement of the molecules involved, making it less sensitive to the surrounding porous medium. This explains the values observed in the graph, which show approximately 2.1 seconds for water relaxation and 0.5 seconds for oil. The $T_1$ relaxation of oil is significantly faster and is associated with differences in molecular properties. In water, hydrogen nuclei wobble too quickly for spins to interact effectively, which leads to longer relaxation times, virtually independent of probing frequency, when compared to hydrocarbon nuclei, which are embedded in a much more viscous fluid [80].

The analysis of $T_2$ relaxation in these fluids is commonly utilized to assess differences in reservoir responses. Since $T_2$ relaxation is more sensitive to pore size and fluid distribution within the porous structure, the $T_2$ values for water and oil are significantly affected. The Figure [3.27] presents the analysis of $T_2$ relaxation for these two fluids within a rock sample, allowing a better understanding of their behavior.

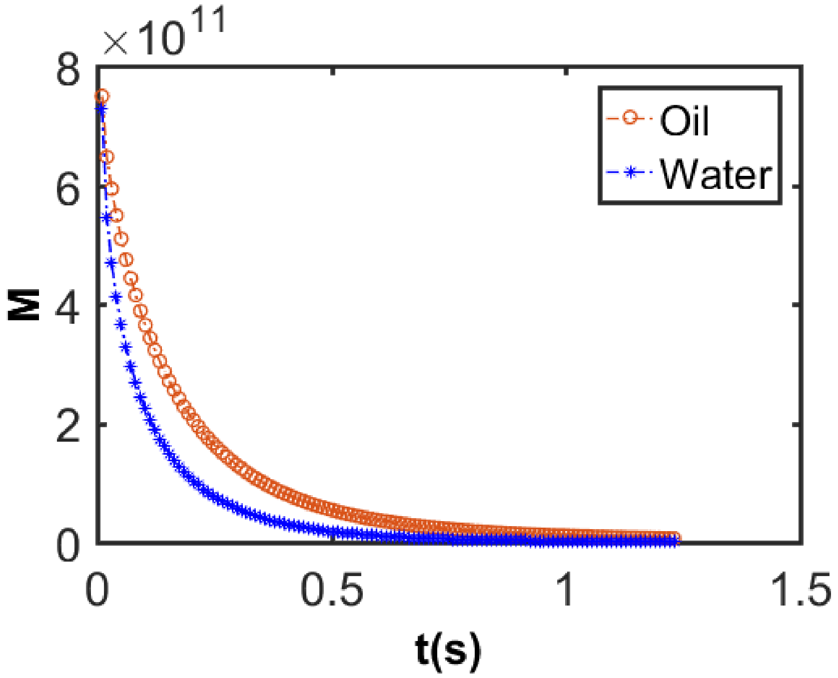

Figure 3.27: $T_2$ relaxation curves for water (blue) and oil (orange) within the rock. The observed relaxation times shows that water relaxes much faster than oil.

As previously discussed, the $T_2$ relaxation curve changes when the fluid in the pore spaces is modified. The figure shows that water relaxes much faster than oil during this process.

The analysis of the relaxation curves revealed distinct behaviors of the fluids when placed in a porous rock, influenced by the magnetic field generated by the NMR equipment. The relaxation times, both $T_1$ and $T_2$, showed significant differences between water and oil, which was crucial for a more accurate analysis of the sample images. This distinction facilitated the identification and quantification of the fluids, enhancing the interpretation of the data obtained through nuclear magnetic resonance.

## 3.6 Image Analysis

Based on the knowledge acquired about the relaxation of these fluids, the images generated by the NMR equipment could be analyzed. Images were acquired from different slices of the sample, with intervals of 0.5 seconds between the time echo, totaling 160 images. Each slice had a thickness of 0.5 $mm$. The Figure [3.28] illustrates the obtained images, allowing for an analysis of the fluid behavior in each slice.

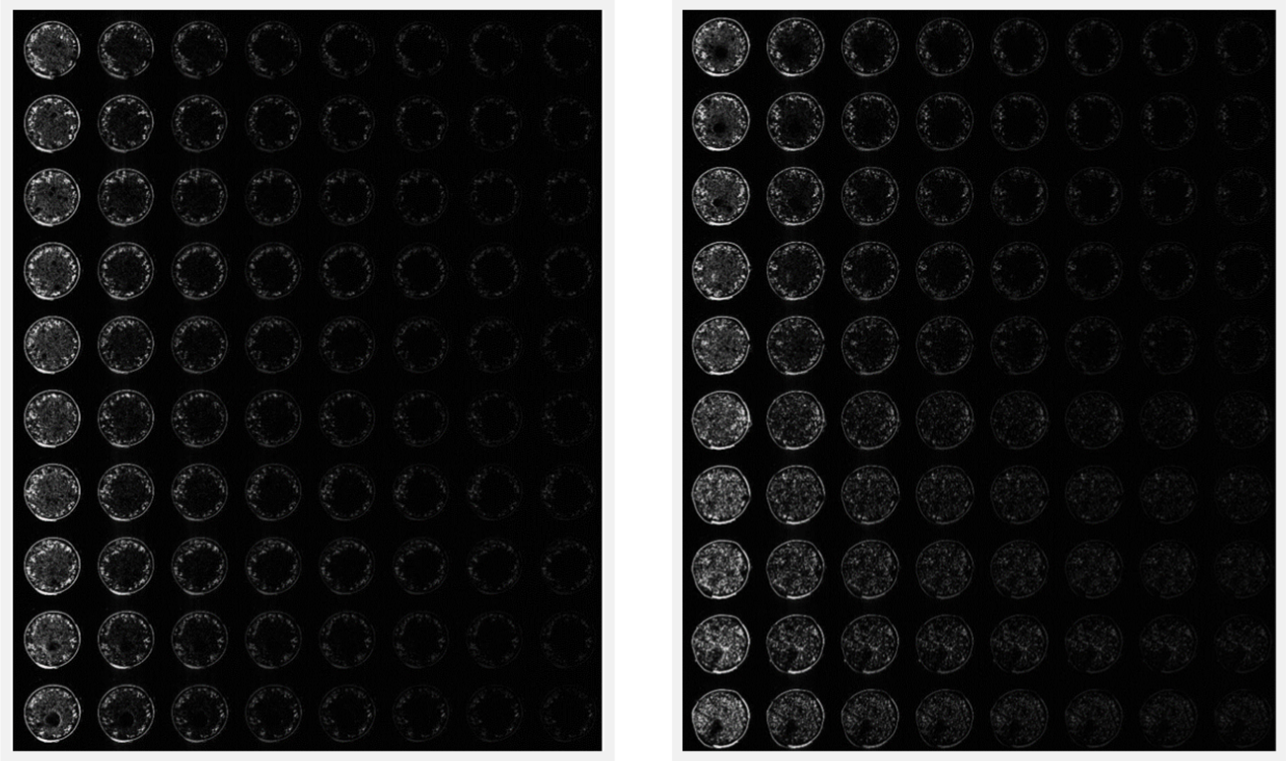

Figure 3.28: NMR images of 20 slices of a sample acquired at 8 different echo times. The variation in contrast across the images reflects differences in the relaxation times of the fluids present in the sample, allowing the characterization of fluid distribution and interaction within the porous sample.

As previously discussed, some parameters are essential to configure the ideal pulse sequence and generate the images. In this case, we used the RARE sequence with $T_2$ weighting. Defining the following values: $N_{ex} = 4$, a 256×256 pixel grid, FOV = 10 $mm$ in XY, a voxel is 80 $\mu m^3$ calculated using the formula (1.12) and resolution of 0.039 $mm$.

For the image acquisition parameters, $TR = 3500ms$ seconds and $TE$ varied between 10 and 150 $ms$ [1]. Twenty slices were acquired with 15 measurements for each slice, aiming to minimize image noise and ensure greater analysis accuracy.

The figure analysis revealed that, over time, one of the fluids exhibited a faster "relaxation" than the other in each slice. Based on the knowledge obtained from the $T_2$ relaxation curves, it was possible to identify that the brightest pixels in the images corresponded to oil due to its more prolonged "disappearance" time, while the more grayish tones indicated the presence of water, this can be seen in the Figure [3.29]. This initial identification of fluids in the images enabled the implementation of a quantification approach based on pixel counting, facilitating accurate analysis of fluid distribution.

---

[1] That is, values of 10, 30, 50, 70, 90, 110, 130, and 150 $ms$, totaling eight steps.

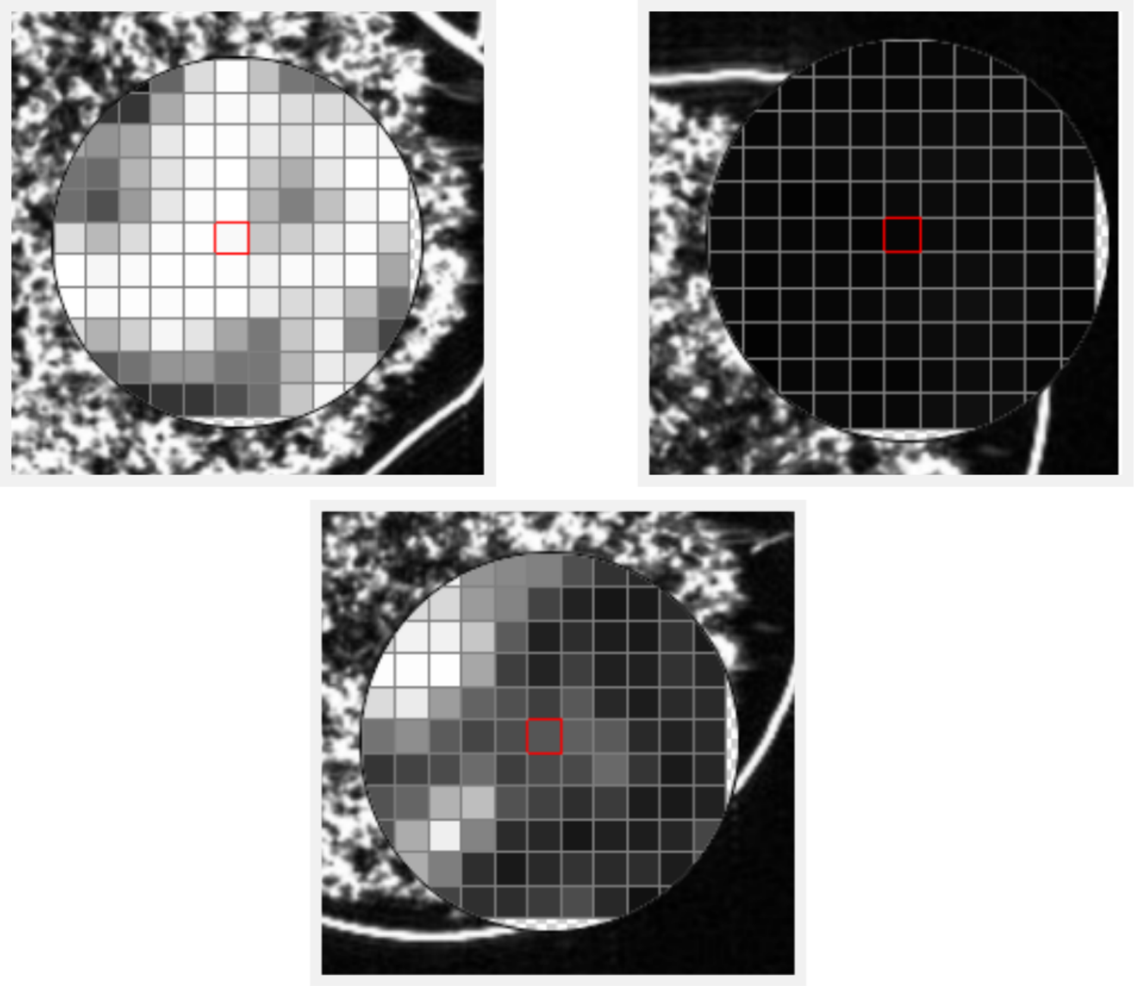

Figure 3.29: Identification of pixel intensity ranges in a rock sample. White pixels represent oil, black pixels correspond to the image background, and gray-scale pixels indicate the presence of water.

All images from the slices corresponding to the initial acquisition time, that is, acquired at the first echo time (TE = 5 $ms$), were selected to initiate the pixel-counting methodology, resulting in a total of 20 images for analysis for each sample. This time point is chosen because these images contain all the information about the fluids before they begin to relax (Figure [3.30]). After selecting the images, an intensity histogram was generated for each one, allowing the analysis of the number of pixels associated with each intensity level, thereby facilitating the quantification and distinction of fluids in the sample.

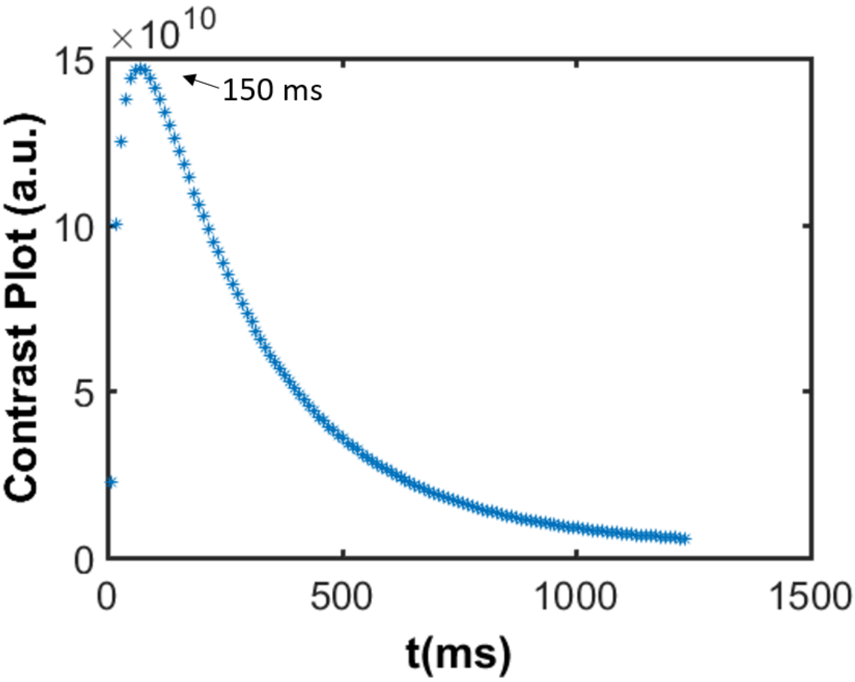

Figure 3.30: A contrast-versus-time curve was obtained to evaluate the temporal behavior of the signal differentiation between fluids. The results indicate an inverse relationship: as the echo time increases, the contrast signal in the generated images gradually decreases.

Specific intensity ranges for each fluid needed to be established to quantify the pixels. The range from 0 to 10 represents the image's background, i.e., all pixels without information about the fluids. The range from 11 to 69 corresponds to water, while the range from 70 to 255 represents oil. These ranges were defined based on a carefully controlled sample throughout the saturation process (Figure [3.31]).

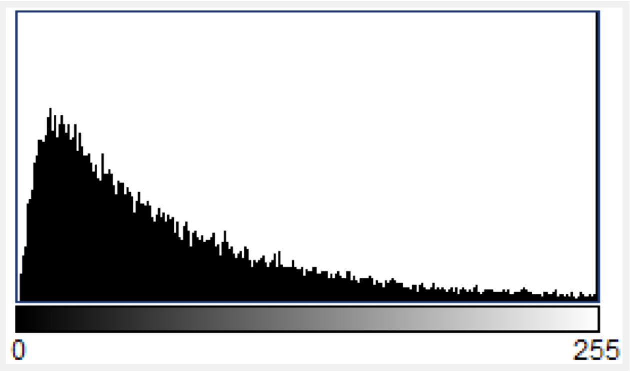

| PARAMETERS | AMS 54 |
|---|---|
| BACKGROUND RANGE | 0-10 |
| WATER RANGE | 11-69 |
| OIL RANGE | 70-255 |

Figure 3.31: Intensity histogram defining pixel ranges for background (0-10), water (11-69), and oil (70-255).

Next, we counted the pixel intensity for each fluid in each sample slice at the first acquisition time. This step aimed to obtain intensity values close to those calculated during the saturation process, thus validating the accuracy of the defined ranges. These ranges were then consistently applied to all other samples.

Therefore, we proceeded with the analysis of sample AMS 54 using the image analysis tool, as described previously, in the following Figure [3.32] :

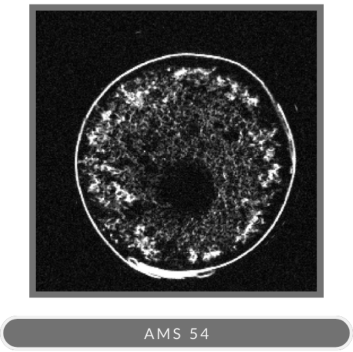

| RANGE | PIXELS | IMAGE ANALYSIS | SATURATION MEASUREMENTS |
|---|---|---|---|
| BG (0-10) | 547.482 | | |
| WATER (11-69) | 395.111 | 77% | 80% |
| OIL (70-255) | 118.509 | 23% | 20% |

| | |
|---|---|
| AVERAGE ERROR | 3% |
| MEAN DEVIATION | 3% |

Figure 3.32: Comparison of fluid quantification methods using pixel classification, image analysis, and saturation measurements. The results show a small error margin (3%) between methods.

Finally, by comparing the pixel intensity values with the data obtained during the saturation measurements, we observed a remarkable correspondence, with an error of less than 5%. This approach's accuracy demonstrates its potential for the practical and reliable quantification of fluids in porous rocks.

# Conclusions

The methodology developed in this study represents a significant advancement in the quantification of immiscible fluids within synthetic porous media, offering valuable contributions to petrophysical characterization and the modeling of multiphase systems. The controlled sintering process using soda-lime glass microspheres enabled the fabrication of samples with physical and chemical properties comparable to natural reservoir rocks, allowing for reproducible and cost-effective laboratory experiments. This approach provides a reliable preliminary stage for testing before engaging with more complex and expensive geological materials.

Furthermore, the proposed protocol opens avenues for the development of novel sintering techniques involving alternative materials—such as the inclusion of clays or silica—to increase structural complexity and enrich analytical depth. The precise control of sintering parameters has proven to be a powerful tool for isolating and investigating specific variables in fluid behavior, particularly in studying water and oil distribution within porous matrices.

From an applied perspective, especially within the petroleum industry, the results indicate considerable potential during critical reservoir evaluation stages. The ability to produce synthetic samples with well-defined and tunable properties could transform workflows in petrophysical studies, flow simulations, and enhanced oil recovery strategies.

A major contribution of this work is the development of a dedicated image analysis algorithm for NMR-based quantification of fluids in porous media. The software demonstrated high accuracy and robustness across diverse experimental conditions, maintaining an average error below 10% and a standard deviation under 5%. These results surpass the performance of conventional methodologies commonly used in the industry, providing a more reliable framework for interpreting images involving weak signals or overlapping fluid phases. This advancement has the potential to support decision-making processes in complex operational environments, such as partially saturated reservoirs and aquifers.

Although the experiments were conducted under controlled laboratory conditions, the results establish a solid foundation for future investigations involving heterogeneous materials, including cement-based composites, clay-rich samples, and natural rock formations. Future developments will focus on incorporating artificial intelligence algorithms into the image analysis tool to enhance its predictive capabilities. By training on previously analyzed datasets, the software is expected to improve performance under low signal-to-noise conditions and expand its applicability to low-field NMR systems and real-world scenarios.

In summary, this study not only validates a novel approach for the analysis and quantification of fluids in porous materials but also opens a promising avenue for scientific and technological innovation in reservoir engineering, materials science, and environmental monitoring.

# Perspectives

The development of the image analysis program based on pixel counting marked a milestone of excellence in this research. It provides excellent reliability in quantifying fluids present in the samples with low error rates. However, challenges still exist to make this approach viable for industrial applications, particularly in the petroleum sector. One of the main improvements needed is optimizing the program for more precise identification of pixels within specific ranges, making the process more efficient and better suited to the industry's reality.

A promising strategy to achieve this enhancement would be implementing artificial intelligence (AI) techniques, which could be integrated into the program to assist in identifying and counting fluids. The program could learn from previously analyzed samples by applying AI, creating more accurate and specific learning models capable of handling a wider range of scenarios and sample conditions. This would enable a more robust and personalized analysis, adapting to the complexities of different types of porous materials.

Another crucial aspect for advancing the methodology would be applying the program to actual rock samples with more complex and varied characteristics. Testing the program with actual samples will validate its effectiveness in more challenging conditions and provide a deeper understanding of how it performs when dealing with the complexities of materials found in the petroleum industry. This practical validation will be essential to establish the program as a reliable and robust tool for petrophysical analyses.

Therefore, the future prospects for this research involve combining technical improvements in the image analysis program with the use of artificial intelligence and its validation in real samples, aiming to expand its applicability and accuracy in the petroleum sector.

# Appendix

In this appendix, all the samples produced, studied, and analyzed during the academic period are compiled, covering the three different granulometries. A detailed description of each sample is provided, including individual characteristics such as dry and wet mass, diameter, height, and porosity. Information related to the saturation process is also presented, including the initial amounts of water and oil, the final quantities of both fluids and their respective percentages.

Furthermore, the appendix includes a comparison of the values of water and oil based on the analyzed images, along with the average errors associated with this process. Echoes for each sample are also provided, offering a more comprehensive view of the measurements performed.

## 3.7 Granulation 1

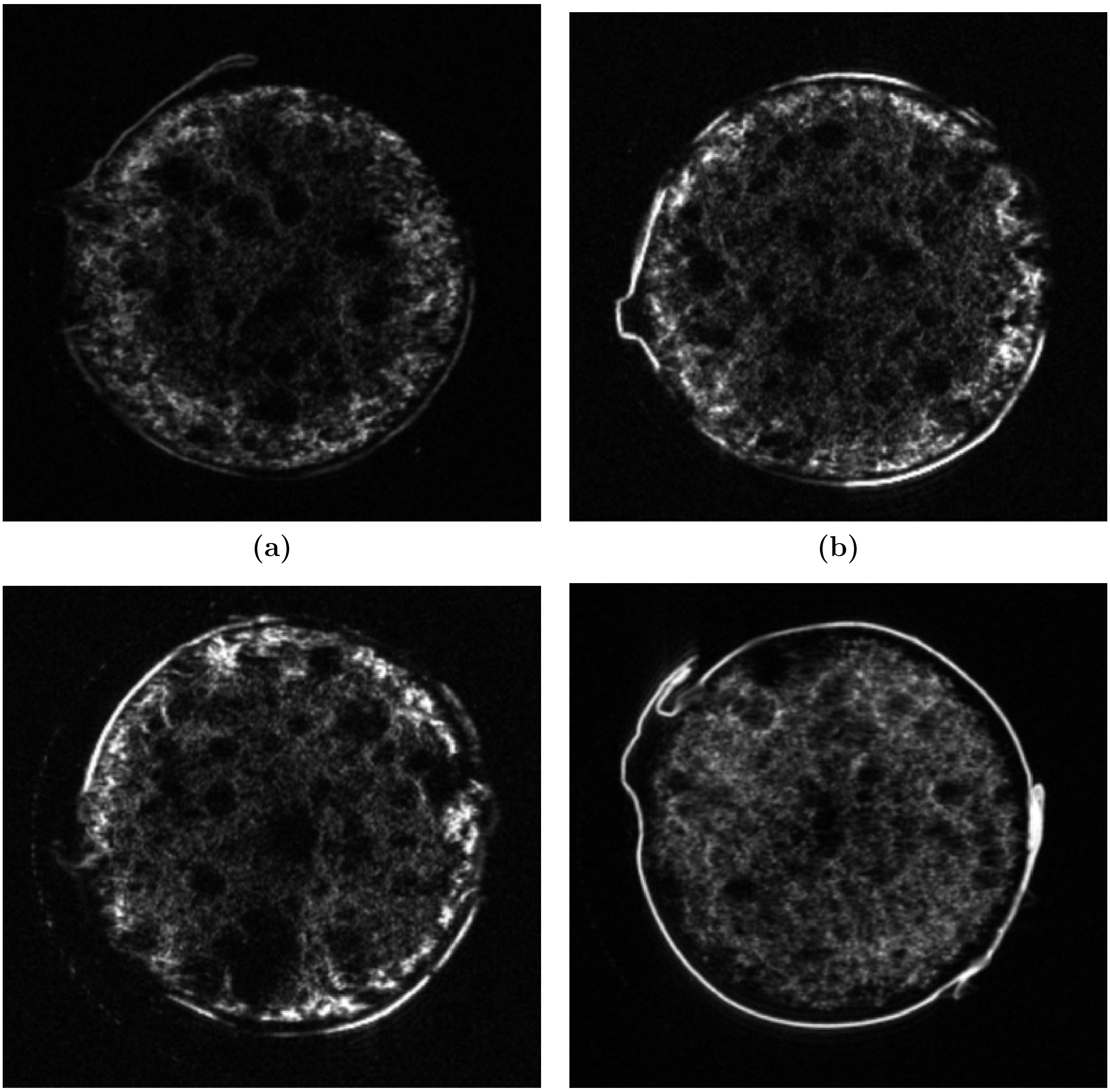

(a) (b) (c) (d)

Figure 3.33: **(a)** Sample 32 **(b)** Sample 33 **(c)** Sample 34 **(d)** Sample 36

| **Parameters** | **AMS 32** | **Parameters** | **AMS 32** |
|---|---|---|---|
| Dry Mass | 2.60 g | Oil that Entered | 10% |
| Wet Mass | 3.17 g | Initial Water Volume | 0.57 ml |
| Diameter | 0.74 cm | Final Water Volume | 0.52 ml |
| Height | 3.90 cm | Oil AMS | 9% |
| Porosity | 66 | Water AMS | 91% |
| Initial Oil Volume | 0.5 ml | Average Error | 4% |
| Final Oil Volume | 0.05 ml | Average Deviation | 2% |

Table 3.6: Fluid saturation parameters of sample AMS 32, including mass, dimensions, porosity, and fluid distribution before and after saturation.

| **Parameters** | **AMS 33** | **Parameters** | **AMS 33** |
|---|---|---|---|
| Dry Mass | 2.55 g | Oil that Entered | 10% |
| Wet Mass | 3.16 g | Initial Water Volume | 0.61 ml |
| Diameter | 0.79 cm | Final Water Volume | 0.51 ml |
| Height | 3.89 cm | Oil AMS | 16% |
| Porosity | 68 | Water AMS | 84% |
| Initial Oil Volume | 1.0 ml | Average Error | 7% |
| Final Oil Volume | 0.10 ml | Average Deviation | 3% |

Table 3.7: Fluid saturation parameters of sample AMS 33, including mass, dimensions, porosity, and fluid distribution before and after saturation.

| **Parameters** | **AMS 34** | **Parameters** | **AMS 34** |
|---|---|---|---|
| Dry Mass | 2.61 g | Oil that Entered | 6% |
| Wet Mass | 3.24 g | Initial Water Volume | 0.63 ml |
| Diameter | 0.72 cm | Final Water Volume | 0.52 ml |
| Height | 3.91 cm | Oil AMS | 17% |
| Porosity | 61 | Water AMS | 83% |
| Initial Oil Volume | 2.0 ml | Average Error | 6% |
| Final Oil Volume | 0.11 ml | Average Deviation | 3% |

Table 3.8: Fluid saturation parameters of sample AMS 34, including mass, dimensions, porosity, and fluid distribution before and after saturation.

| **Parameters** | **AMS 36** | **Parameters** | **AMS 36** |
|---|---|---|---|
| Dry Mass | 2.57 g | Oil that Entered | 5% |
| Wet Mass | 3.14 g | Initial Water Volume | 0.56 ml |
| Diameter | 0.74 cm | Final Water Volume | 0.40 ml |
| Height | 3.91 cm | Oil AMS | 29% |
| Porosity | 67 | Water AMS | 71% |
| Initial Oil Volume | 3.0 ml | Average Error | 6% |
| Final Oil Volume | 0.16 ml | Average Deviation | 4% |

Table 3.9: Fluid saturation parameters of sample AMS 36, including mass, dimensions, porosity, and fluid distribution before and after saturation.

## 3.8 Granulation 2

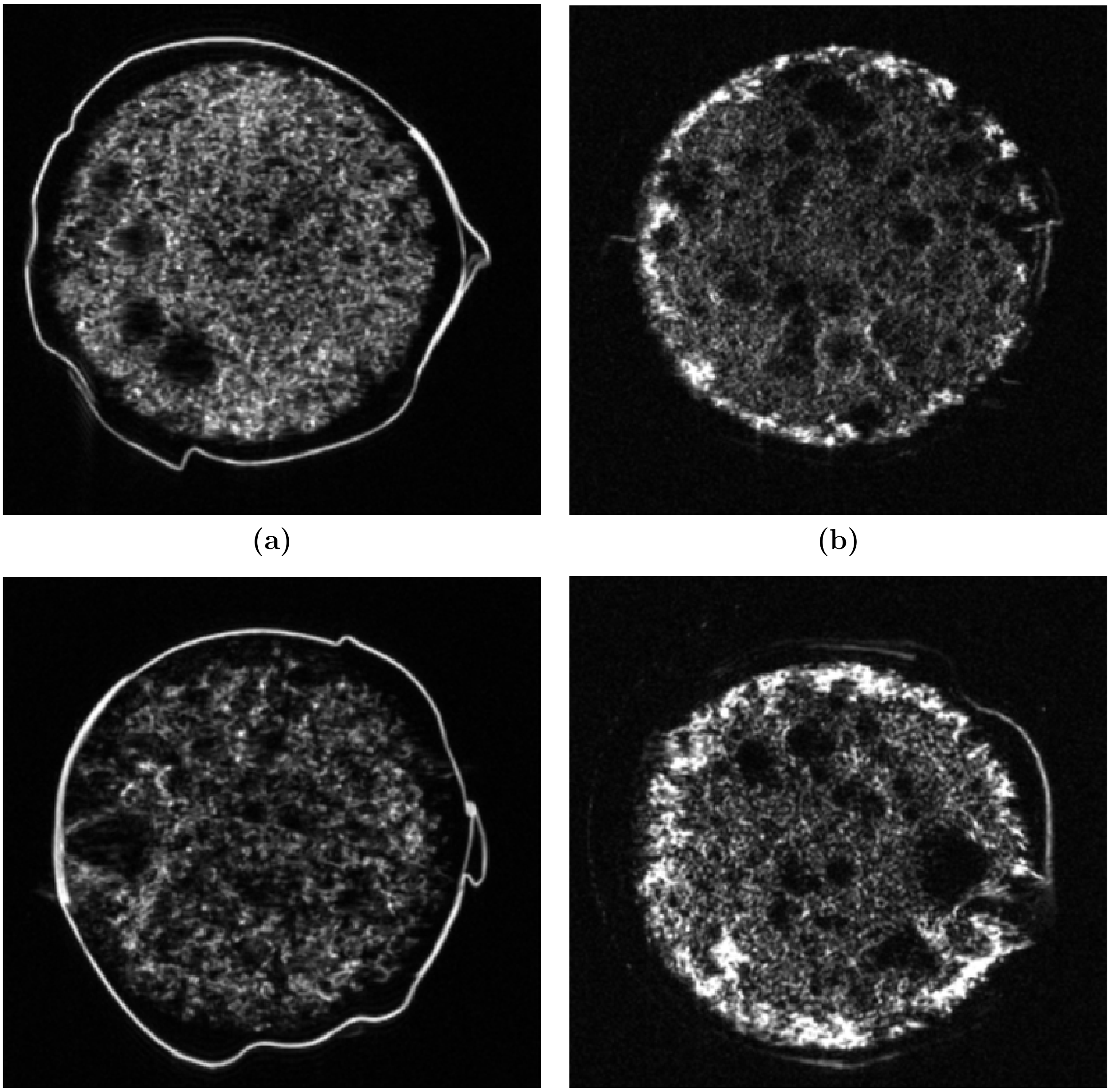

(a) (b) (c) (d)

Figure 3.34: **(a)** Sample 28 **(b)** Sample 29 **(c)** Sample 30 **(d)** Sample 31

| **Parameters** | **AMS 28** | **Parameters** | **AMS 28** |
|---|---|---|---|
| Dry Mass | 2.61 g | Oil that Entered | 18% |
| Wet Mass | 3.11 g | Initial Water Volume | 0.49 ml |
| Diameter | 0.74 cm | Final Water Volume | 0.31 ml |
| Height | 3.87 cm | Oil AMS | 37% |
| Porosity | 71 | Water AMS | 63% |
| Initial Oil Volume | 1.0 ml | Average Error | 7% |
| Final Oil Volume | 0.18 ml | Average Deviation | 5% |

Table 3.10: Fluid saturation parameters of sample AMS 28, including mass, dimensions, porosity, and fluid distribution before and after saturation.

| **Parameters** | **AMS 29** | **Parameters** | **AMS 29** |
|---|---|---|---|
| Dry Mass | 2.58 g | Oil that Entered | 4% |
| Wet Mass | 3.21 g | Initial Water Volume | 0.63 ml |
| Diameter | 0.74 cm | Final Water Volume | 0.61 ml |
| Height | 3.92 cm | Oil AMS | 3% |
| Porosity | 63 | Water AMS | 97% |
| Initial Oil Volume | 0.5 ml | Average Error | 6% |
| Final Oil Volume | 0.02 ml | Average Deviation | 4% |

Table 3.11: Fluid saturation parameters of sample AMS 29, including mass, dimensions, porosity, and fluid distribution before and after saturation.

| **Parameters** | **AMS 30** | **Parameters** | **AMS 30** |
|---|---|---|---|
| Dry Mass | 2.60 g | Oil that Entered | 9% |
| Wet Mass | 3.18 g | Initial Water Volume | 0.57 ml |
| Diameter | 0.74 cm | Final Water Volume | 0.39 ml |
| Height | 3.93 cm | Oil AMS | 32% |
| Porosity | 66 | Water AMS | 68% |
| Initial Oil Volume | 2.0 ml | Average Error | 6% |
| Final Oil Volume | 0.18 ml | Average Deviation | 4% |

Table 3.12: Fluid saturation parameters of sample AMS 30, including mass, dimensions, porosity, and fluid distribution before and after saturation.

| **Parameters** | **AMS 31** | **Parameters** | **AMS 31** |
|---|---|---|---|
| Dry Mass | 2.52 g | Oil that Entered | 7% |
| Wet Mass | 3.05 g | Initial Water Volume | 0.52 ml |
| Diameter | 0.74 cm | Final Water Volume | 0.35 ml |
| Height | 3.82 cm | Oil AMS | 33% |
| Porosity | 68 | Water AMS | 67% |
| Initial Oil Volume | 3.0 ml | Average Error | 8% |
| Final Oil Volume | 0.17 ml | Average Deviation | 2% |

Table 3.13: Fluid saturation parameters of sample AMS 31, including mass, dimensions, porosity, and fluid distribution before and after saturation.

## 3.9 Granulation 3

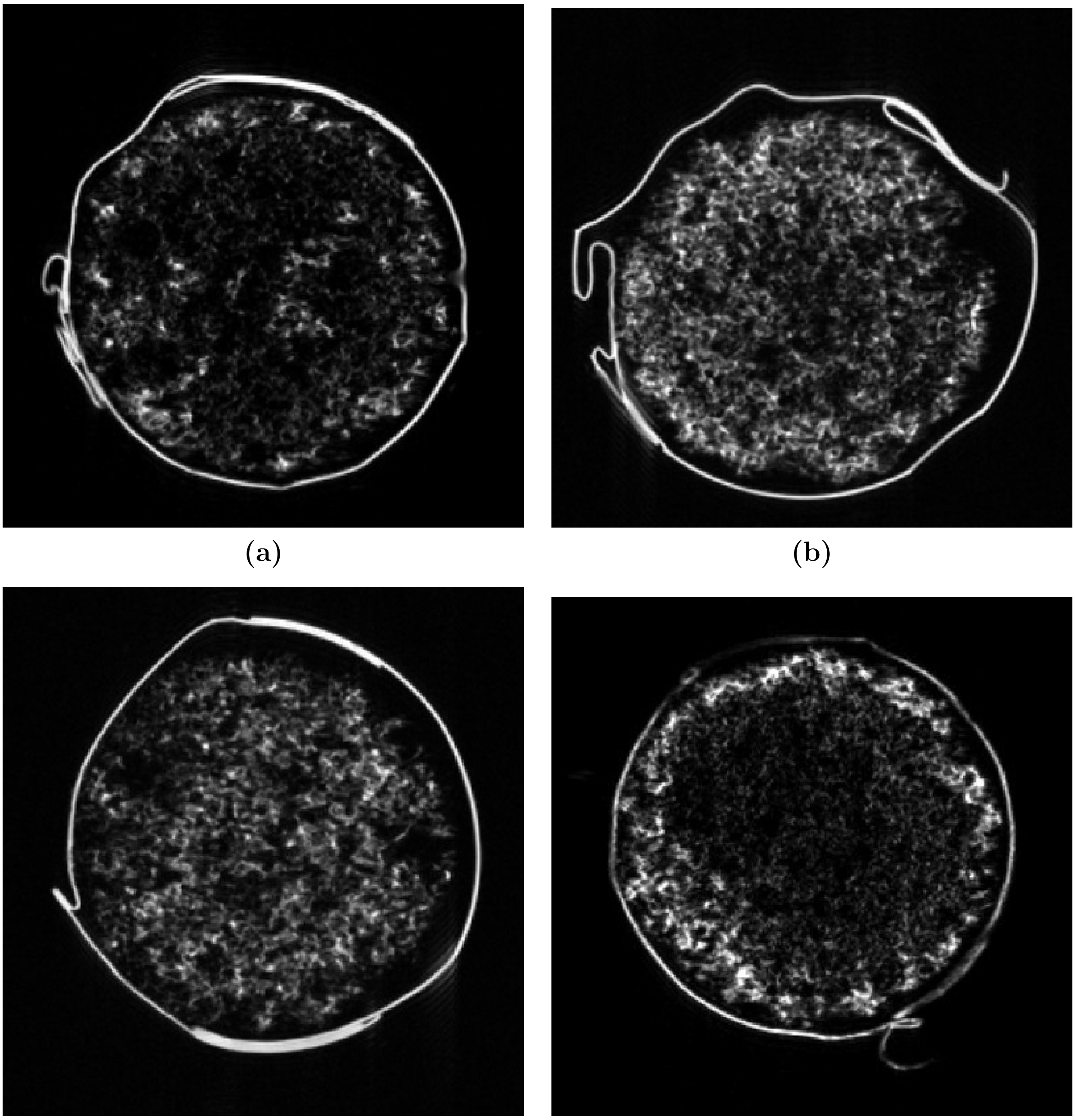

(a) (b)

(c) (d)

Figure 3.35: **(a)** Sample 18 **(b)** Sample 19 **(c)** Sample 20 **(d)** Sample 21

| **Parameters** | **AMS 18** | **Parameters** | **AMS 18** |
|---|---|---|---|
| Dry Mass | 2.35 g | Oil that Entered | 60% |
| Wet Mass | 2.96 g | Initial Water Volume | 0.61 ml |
| Diameter | 0.74 cm | Final Water Volume | 0.31 ml |
| Height | 3.67 cm | Oil AMS | 49% |
| Porosity | 62 | Water AMS | 51% |
| Initial Oil Volume | 0.5 ml | Average Error | 2% |
| Final Oil Volume | 0.30 ml | Average Deviation | 4% |

Table 3.14: Fluid saturation parameters of sample AMS 18, including mass, dimensions, porosity, and fluid distribution before and after saturation.

| **Parameters** | **AMS 19** | **Parameters** | **AMS 19** |
|---|---|---|---|
| Dry Mass | 2.55 g | Oil that Entered | 10% |
| Wet Mass | 3.14 g | Initial Water Volume | 0.58 ml |
| Diameter | 0.75 cm | Final Water Volume | 0.28 ml |
| Height | 3.88 cm | Oil AMS | 54% |
| Porosity | 66 | Water AMS | 46% |
| Initial Oil Volume | 3.0 ml | Average Error | 6% |
| Final Oil Volume | 0.30 ml | Average Deviation | 4% |

Table 3.15: Fluid saturation parameters of sample AMS 19, including mass, dimensions, porosity, and fluid distribution before and after saturation.

| **Parameters** | **AMS 20** | **Parameters** | **AMS 20** |
|---|---|---|---|
| Dry Mass | 2.35 g | Oil that Entered | 28% |
| Wet Mass | 2.86 g | Initial Water Volume | 0.50 ml |
| Diameter | 0.74 cm | Final Water Volume | 0.22 ml |
| Height | 3.71 cm | Oil AMS | 56% |
| Porosity | 69 | Water AMS | 44% |
| Initial Oil Volume | 1.0 ml | Average Error | 5% |
| Final Oil Volume | 0.28 ml | Average Deviation | 4% |

Table 3.16: Fluid saturation parameters of sample AMS 20, including mass, dimensions, porosity, and fluid distribution before and after saturation.

| **Parameters** | **AMS 21** | **Parameters** | **AMS 21** |
|---|---|---|---|
| Dry Mass | 2.36 g | Oil that Entered | 16% |
| Wet Mass | 2.90 g | Initial Water Volume | 0.54 ml |
| Diameter | 0.74 cm | Final Water Volume | 0.22 ml |
| Height | 3.73 cm | Oil AMS | 59% |
| Porosity | 67 | Water AMS | 41% |
| Initial Oil Volume | 2.0 ml | Average Error | 6% |
| Final Oil Volume | 0.32 ml | Average Deviation | 4% |

Table 3.17: Fluid saturation parameters of sample AMS 21, including mass, dimensions, porosity, and fluid distribution before and after saturation.

# Events and Conferences

This chapter will be dedicated to reporting all the events and conferences I participated in during my master's, with the goal of disseminating the knowledge generated by my research and contributing to the advancement of the field. Throughout this journey, I sought to present and discuss my findings, interact with experts and researchers from different parts of the world, and expand my academic and professional network. Participation in relevant events was essential not only to enhance my scientific communication skills but also to receive valuable feedback, establish partnerships, and explore new perspectives on the topics I have been researching. Moreover, these events provided a platform for exchanging ideas and staying updated on the latest advancements in the field of nuclear magnetic resonance (NMR) and its application in the characterization of porous materials and the study of fluids in reservoirs.

1. **2024 Autumn Meeting of the Brazilian Physical Society**
   *Presentation*: Poster on *Sintering of Porous Rocks and Petrophysical Analysis by Nuclear Magnetic Resonance*
   *Year*: 2024
   *Type*: Conference
   *Award*: Best Poster in the Industry Physics category

2. **3rd Workshop on New Applications of Nuclear Magnetic Resonance (NMR) in Low Field**
   *Presentation*: Oral Presentation on *Determination of Fluid Content in Porous Rocks from NMR Images*
   *Year*: 2024
   *Type*: Conference

3. **Escola de Física Experimental (EAFEXP) 7 CBPF**
   *Presentation*: Poster on *Sintering of Porous Rocks and Petrophysical Analysis by Nuclear Magnetic Resonance*
   *Year*: 2024
   *Type*: Workshop

4. **Society of Petrophysical and Well Log Analysts (SPWLA) Brazil**
   *Course*: Course on *Nuclear Magnetic Resonance in Formation Evaluation*
   *Year*: 2024
   *Type*: Workshop

5. **XIV CBPF School**
   *Presentation*: Poster
   *Year*: 2023
   *Type*: Conference

6. **COMAN Conference at CBPF**
   *Presentation*: Poster on *Sintering of Porous Rocks and Petrophysical Analysis by Nuclear Magnetic Resonance*
   *Year*: 2023
   *Type*: Conference

# Bibliography

[1] Yi-Qiao Song. Magnetic resonance of porous media (mrpm): A perspective. *Journal of Magnetic Resonance*, 229:12–24, 2013. Frontiers of In Vivo and Materials MRI Research.

[2] Srinath V. Ekkad and Prashant Singh. Chapter six - recent advancements in single-phase liquid-based heat transfer in microchannels. volume 55 of *Advances in Heat Transfer*, pages 239–293. Elsevier, 2023.

[3] Nobel Prize Organization. Felix Bloch - Biographical, 1952. [Accessed: 2024-11-07].

[4] F. Bloch. Nuclear relaxation in gases by surface catalysis. *Phys. Rev.*, 83:1062–1063, Sep 1951.

[5] John Mitchell and Luiz F. Gladden. *Nuclear Magnetic Resonance: Principles and Applications.* Royal Society of Chemistry, Cambridge, UK, 2013.

[6] Petrobras. Pré-Sal. [Accessed: 2024-11-07].

[7] Abhijit Y. Dandekar. *Petroleum Reservoir Rock and Fluid Properties.* CRC Press, Boca Raton, FL, 2006.

[8] Jürgen H. Schön. Chapter 3 - nuclear magnetic resonance (nmr): Petrophysical properties. In Jürgen H. Schön, editor, *Physical Properties of Rocks*, volume 65 of *Developments in Petroleum Science*, pages 85–107. Elsevier, 2015.

[9] Pedram Masoudi. *Analysing spatialized data: applications of geo-datasciences in geophysics and petroleum industry.* Habilitation à diriger des recherches, Université Paris-Saclay, March 2024.

[10] Sébastien Simon, Andreas L. Nenningsland, Emily Herschbach, and Johan Sjöblom. Extraction of basic components from petroleum crude oil. *Energy & Fuels*, 24(2):1043–1050, 2010.

[11] B. Helmi-Oskoui, R. Narayanan, T. Glover, K.S. Lyon, and M. Sinha. Optimal extraction of petroleum resources: An empirical approach. *Resources and Energy*, 14(3):267–285, 1992.

[12] Bloch. Nuclear induction. *Phys. Rev.*, 69:127–127, Feb 1946.

[13] Purcell. Resonance absorption by nuclear magnetic moments in a solid. *Phys. Rev.*, 69:37–38, Jan 1946.

[14] Tal Geva. Magnetic resonance imaging: historical perspective. *Journal of cardiovascular magnetic resonance*, 8(4):573–580, 2006.

[15] E. O. Stejskal and J. E. Tanner. Spin diffusion measurements: Spin echoes in the presence of time-dependent field gradient. *The Journal of Chemical Physics*, 42(1):288–292, 1965.

[16] P. C. Lauterbur. Image formation by induced local interactions: Examples employing nuclear magnetic resonance. *Nature*, 242(5394):190–191, 1973.

[17] Peter Mansfield and Andrew A. Maudsley. Multi-planar image formation using nmr spin echoes. *Journal of Physics C: Solid State Physics*, 10(3):L55–L58, 1977.

[18] The Nobel Assembly at Karolinska Institute. The nobel prize in physiology or medicine 2003. `https://www.nobelprize.org/prizes/medicine/2003/7453-the-nobel-prize-in-physiology-or-medicine-2003-2003/#:~:text=The%20Nobel%20Assembly%20at%20Karolinska,concerning%20œmagnetic%20resonance%20imaging`, 2003. Accessed: 2025-03-10.

[19] R. R. Ernst, G. Bodenhausen, and A. Wokaun. *Principles of Nuclear Magnetic Resonance in One and Two Dimensions.* Clarendon Press, 1987.

[20] C. P. Slichter. *Principles of Magnetic Resonance.* Springer, 1990.

[21] P. T. Callaghan. *Principles of Nuclear Magnetic Resonance Microscopy.* Clarendon Press, 1991.

[22] F. Bloch. Nuclear induction. *Physical Review*, 70(7-8):460–474, 1946.

[23] A. Abragam. *The Principles of Nuclear Magnetism.* Clarendon Press, 1961.

[24] M. H. Levitt. *Spin Dynamics: Basics of Nuclear Magnetic Resonance.* Wiley, 2001.

[25] P. S. Hall and T. J. Wong. *NMR: The Toolkit.* Oxford University Press, Oxford, 2007.

[26] H. Y. Carr. *Principles of Nuclear Magnetic Resonance in One and Two Dimensions.* W. A. Benjamin, Inc., New York, 1972.

[27] R. Freeman. *Principles of Nuclear Magnetic Resonance.* Oxford University Press, Oxford, 1998.

[28] E. M. Purcell, H. C. Torrey, and R. V. Pound. *Nuclear Magnetic Resonance*, volume 69. 1951.

[29] E. Mark Haacke, Robert W. Brown, Michael R. Thompson, and Ramesh Venkatesan. *Magnetic Resonance Imaging: Physical Principles and Sequence Design.* Wiley-Liss, New York, 1999.

[30] D. G. Cory and R. M. Pielak. *Introduction to Magnetic Resonance with Applications in Chemistry and Chemical Engineering.* Wiley-Interscience, New York, 1990.

[31] A. Schweiger. *Principles of Magnetic Resonance.* Oxford University Press, Oxford, 2001.

[32] Charles P. Poole. *Electron Spin Resonance: A Comprehensive Treatise on Experimental Techniques.* Dover Publications, Mineola, NY, 2nd edition, 1997.

[33] Howard Grad and Norman M. Alpert. Effect of inhomogeneous magnetic fields on spin echoes and nuclear magnetic resonance relaxation times. *Physical Review*, 141(2):321–329, 1966.

[34] H. Y. Carr and E. M. Purcell. Effects of diffusion on free precession in nuclear magnetic resonance experiments. *Physical Review*, 94(3):630–638, 1954.

[35] Timothy D.W. Claridge. *High-Resolution NMR Techniques in Organic Chemistry*, volume 27 of *Tetrahedron Organic Chemistry Series.* Elsevier, 3rd edition, 2016.

[36] Paul T. Callaghan. *Principles of Nuclear Magnetic Resonance Microscopy.* Oxford University Press, 1993.

[37] S. K. Ferguson and A. N. Hasso. *Magnetic Resonance Imaging: A Guide for Physicians.* Elsevier, 2009.

[38] M. Wood and A. M. Blamire. *Magnetic Resonance Imaging: Physical and Biological Principles*. Wiley-Liss, 2007.

[39] Christian A. Helsen, Yannick Boulanger, Julien M. Wolber, and Derek A. Turek. Pulse sequences and their role in magnetic resonance imaging: Basic principles and applications. *Journal of Magnetic Resonance Imaging*, 45(6):1593–1608, 2017.

[40] Manfred Haegele and Mark E. Ladd. *Principles of Magnetic Resonance Imaging: Physics and Applications*. Springer, Berlin, 2nd edition, 2016.

[41] Michael A. Bernstein, John R. King, and Xiaodong Zhou. *Handbook of MRI Pulse Sequences*. Elsevier, San Diego, 1st edition, 2004.

[42] Robert B. Lauffer and Derek W. Bessette. *Principles of Magnetic Resonance Imaging: A Conceptual Approach*. Wiley-Liss, Hoboken, 1st edition, 2010.

[43] Peter T. Callaghan. *Principles of Nuclear Magnetic Resonance Microscopy*. Oxford University Press, Oxford, 1st edition, 2011.

[44] William M. Wells, Ivan Viola, and Ron Kikinis. *Principles of Medical Imaging*. Academic Press, San Diego, 1st edition, 2014.

[45] John R. King, Jonathan Gray, and John F. Wilson. *Magnetic Resonance Imaging: Principles and Techniques*. Cambridge University Press, Cambridge, 1st edition, 2003.

[46] Manfred Haegele and Mark E. Ladd. *Magnetic Resonance Imaging: Principles and Techniques*. Springer, Berlin, 1st edition, 2004.

[47] Adam D. Elster and Paul C. Lauterbur. *Principles of Magnetic Resonance Imaging: A Teaching Manual*. Springer, New York, 1st edition, 2012.

[48] M. H. Levitt. *Spin Dynamics*. John Wiley & Sons Ltd., 2008.

[49] M. A. Bernstein, K. E. King, X. J. Zhou, and W. Fong. *Handbook of MRI Pulse Sequences*. Elsevier, 2004. Retrieved 2008-04-08.

[50] Jürgen Hennig, Andreas Nauerth, and Helmut Friedburg. Rare imaging: A fast imaging method for clinical mr. *Magnetic Resonance in Medicine*, 3(6):823–833, 1986.

[51] E. M. Purcell, H. C. Torrey, and R. V. Pound. *Resonance Absorption by Nuclear Magnetic Moments in a Solid*, volume 69. 1950.

[52] Society of Petroleum Engineers. *Petrophysics.* Elsevier, 2017.

[53] Elsevier. *Developments in Petroleum Science, Volume 62.* Elsevier, 2015.

[54] Elsevier. *Petrophysical Characterization and Fluids Transport in Unconventional Reservoirs.* Elsevier, 2019.

[55] F. Jerry Lucia. *Petrophysical Rock Properties*, pages 1–27. Springer Berlin Heidelberg, Berlin, Heidelberg, 2007.

[56] G. R. Coates, L. Xiao, and M. G. Prammer. *NMR Logging: Principles and Applications.* Gulf Professional Publishing, Houston, Texas, 1999.

[57] Maurice E. Tucker. *Sedimentary Petrology: An Introduction to the Origin of Sedimentary Rocks.* Blackwell Science, Oxford, 3rd edition, 2001.

[58] Djebbar Tiab and Erle C. Donaldson. *Petrophysics: Theory and Practice of Measuring Reservoir Rock and Fluid Transport Properties.* Gulf Professional Publishing, Oxford, 4th edition, 2015.

[59] Larry W. Lake, Mark P. Walsh, and T. S. Ramakrishnan. *Fundamentals of Enhanced Oil Recovery.* Society of Petroleum Engineers, Richardson, TX, 2nd edition, 2014.

[60] Schlumberger. *Log Interpretation Principles/Applications.* Schlumberger Educational Services, Houston, TX, 1989.

[61] Henry Darcy. *Les fontaines publiques de la ville de Dijon.* Victor Dalmont, Paris, 1856. Includes Darcy's law, which describes the flow of fluids through porous media.

[62] Ronald A. Nelson. *Geologic Analysis of Naturally Fractured Reservoirs.* Gulf Professional Publishing, Oxford, 2nd edition, 2009.

[63] B.C. Craft, M.F. Hawkins, and R.E. Terry. *Applied Petroleum Reservoir Engineering.* Prentice Hall, Englewood Cliffs, NJ, 2nd edition, 1991.

[64] S. M. Auerbach, N. R. Morrow, and R. S. Schechter. *Wettability: Interdisciplinary Contributions.* Springer, Berlin, 2002.

[65] N. R. Morrow. *Wettability in Oil Reservoirs.* Society of Petroleum Engineers, Richardson, TX, 1990.

[66] R. Baker, A. Zaitoun, and M. Dykstra. Wettability and its effect on oil recovery. *Journal of Petroleum Technology*, 40(3):350–358, 1988.

[67] S. E. Buckley and M. C. Leverett. *Capillary Pressure in Porous Media.* Society of Petroleum Engineers, Richardson, TX, 1990.

[68] M. Chandler and L. Peterson. *Mercury Intrusion Porosimetry: A Literature Review.* Elsevier, Amsterdam, 2004.

[69] H. E. Hilton and R. McCaffrey. *Fluid Flow and Transport in Rocks: From Theory to Applications.* Springer, Berlin, 2014.

[70] R. W. Zimmerman and G. S. Bodvarsson. *Fluid Flow and Transport in Rocks: From Theory to Applications.* Springer, Berlin, 2015.

[71] A. Unlu and I. Y. Akkutlu. *Geomechanics of Oil Reservoirs: Rock Mechanics, Reservoir Characterization, and Drilling.* Springer, Cham, 2015.

[72] Bruno Chencarek. Processo para produção e caracterização de rochas sintéticas com porosidade controlada para aplicações em petrofísica por rmn de alto e baixo campo, 2017. Master's dissertation, Centro Brasileiro de Pesquisas Físicas.

[73] Instituto de Geociências da USP. Rochas Ígneas. `https://didatico.igc.usp.br/rochas/igneas/`, n.d. Accessed: 2024-09-25.

[74] J. J. Newby, M. A. Legg, B. Rogers, and M. J. Wirth. Annealing of silica to reduce the concentration of isolated silanols and peak tailing in reverse phase liquid chromatography. *Journal of Chromatography A*, 1218(31):5131–5135, Aug 2011.

[75] Carbolite Gero. Fornos de câmara - detalhes técnicos, 2024. Accessed: 2024-09-25.

[76] V. G. Lifshits, I. G. Kaverina, V. V. Korobtsov, A. A. Saranin, and A. V. Zotov. Thermal annealing behaviour of si/sio2 structures. *Thin Solid Films*, 135:99–105, 1986. Received August 21, 1984; revised March 22, 1985; accepted May 8, 1985.

[77] Tarek Ahmed. *Reservoir Engineering Handbook.* Gulf Professional Publishing, Burlington, MA, 4th edition, 2010.

[78] Petrobras. Produtos do dia a dia e petroquímicos: conheça os principais derivados do petróleo, 2024. [Accessed: 2024-11-07].

[79] V. Jahanvi and A. Kelkar. Chemical shift imaging: An indispensable tool in diagnosing musculoskeletal pathologies. *SA Journal of Radiology*, 25(1):2061, 2021.

[80] Brian Cowan. *Nuclear Magnetic Resonance and Relaxation*. Cambridge University Press, Cambridge, 1997.